

# INTERSTELLAR CN AND CH<sup>+</sup> IN DIFFUSE MOLECULAR CLOUDS: <sup>12</sup>C/<sup>13</sup>C RATIOS AND CN EXCITATION<sup>1</sup>

A. M. RITCHEY<sup>2,3</sup>, S. R. FEDERMAN<sup>2,3</sup>, AND D. L. LAMBERT<sup>4</sup>

*Draft version October 30, 2018*

## ABSTRACT

We present very high signal-to-noise ratio absorption-line observations of CN and CH<sup>+</sup> along 13 lines of sight through diffuse molecular clouds. The data are examined to extract precise isotopologic ratios of <sup>12</sup>CN/<sup>13</sup>CN and <sup>12</sup>CH<sup>+</sup>/<sup>13</sup>CH<sup>+</sup> in order to assess predictions of diffuse cloud chemistry. Our results on <sup>12</sup>CH<sup>+</sup>/<sup>13</sup>CH<sup>+</sup> confirm that this ratio does not deviate from the ambient <sup>12</sup>C/<sup>13</sup>C ratio in local interstellar clouds, as expected if the formation of CH<sup>+</sup> involves nonthermal processes. We find that <sup>12</sup>CN/<sup>13</sup>CN, however, can be significantly fractionated away from the ambient value. The dispersion in our sample of <sup>12</sup>CN/<sup>13</sup>CN ratios is similar to that found in recent surveys of <sup>12</sup>CO/<sup>13</sup>CO. For sight lines where both ratios have been determined, the <sup>12</sup>CN/<sup>13</sup>CN ratios are generally fractionated in the opposite sense compared to <sup>12</sup>CO/<sup>13</sup>CO. Chemical fractionation in CO results from competition between selective photodissociation and isotopic charge exchange. An inverse relationship between <sup>12</sup>CN/<sup>13</sup>CN and <sup>12</sup>CO/<sup>13</sup>CO follows from the coexistence of CN and CO in diffuse cloud cores. However, an isotopic charge exchange reaction with CN may mitigate the enhancements in <sup>12</sup>CN/<sup>13</sup>CN for lines of sight with low <sup>12</sup>CO/<sup>13</sup>CO ratios. For two sight lines with high values of <sup>12</sup>CO/<sup>13</sup>CO, our results indicate that about 50% of the carbon is locked up in CO, which is consistent with the notion that these sight lines probe molecular cloud envelopes where the transition from C<sup>+</sup> to CO is expected to occur. An analysis of CN rotational excitation yields a weighted mean value for T<sub>01</sub>(<sup>12</sup>CN) of 2.754 ± 0.002 K, which implies an excess over the temperature of the cosmic microwave background of only 29 ± 3 mK. This modest excess eliminates the need for a local excitation mechanism beyond electron and neutral collisions. The rotational excitation temperatures in <sup>13</sup>CN show no excess over the temperature of the CMB.

*Subject headings:* ISM: abundances — ISM: clouds — ISM: molecules

## 1. INTRODUCTION

The <sup>12</sup>C-to-<sup>13</sup>C isotopic ratio in the interstellar medium (ISM) is an important diagnostic for probing the history of nucleosynthesis and chemical enrichment in the Galaxy. The abundance of <sup>13</sup>C increases relative to <sup>12</sup>C over Galactic timescales because <sup>13</sup>C is a secondary product of stellar nucleosynthesis. Moreover, millimeter-wave emission studies of CO (Langer & Penzias 1990), H<sub>2</sub>CO (Henkel et al. 1982), and CN (Savage et al. 2002; Milam et al. 2005) in dense molecular clouds have demonstrated the existence of a Galactic gradient in the <sup>12</sup>C/<sup>13</sup>C ratio, with increasingly lower values found closer to the Galactic center (see also the reviews by Wilson & Rood 1994 and Wilson 1999). The increase in <sup>12</sup>C/<sup>13</sup>C with Galactocentric distance presumably reflects the reduced rates of star formation, and subsequent stellar nucleosynthesis and mass loss, that are characteristic of the outer Galactic disk. The enrichment process, acting over the 4.6 Gyr since the formation of the solar system, also offers a natural explanation for the reduction in the <sup>12</sup>C/<sup>13</sup>C

ratio in the vicinity of the Sun. The terrestrial value of <sup>12</sup>C/<sup>13</sup>C, which should approximate the interstellar value at the time of collapse of the solar nebula, is 89 (Lodders 2003), while values close to 70 are typical of local interstellar clouds. Estimates for the present-day, local ISM value of <sup>12</sup>C/<sup>13</sup>C are usually obtained from absorption or emission studies of carbon-bearing molecules, which serve as proxies when direct measurements of the ambient carbon isotopic ratio are lacking. Wilson (1999), for example, derived an average <sup>12</sup>C/<sup>13</sup>C ratio of 69 ± 6 from millimeter-wave data on CO and H<sub>2</sub>CO emission for 13 local sources. More recently, Milam et al. (2005) added millimeter observations of CN in dense clouds to those of CO and H<sub>2</sub>CO and found an average for the present-day, local <sup>12</sup>C/<sup>13</sup>C ratio of 68 ± 15. In this paper, we shall follow Sheffer et al. (2007) and take the ambient <sup>12</sup>C/<sup>13</sup>C ratio in the solar neighborhood to be 70 ± 7 (see also Sheffer et al. 2002).

When molecular proxies are used to evaluate the interstellar abundance ratio of <sup>12</sup>C to <sup>13</sup>C, the values sometimes show evidence of chemical fractionation. While this is generally not the case in dense molecular clouds, where the processes responsible for fractionation are less effective (see Milam et al. 2005), fractionation can have a significant impact in diffuse clouds. Detailed models predict that the fractionation processes in diffuse environments will not affect each interstellar molecule in the same way. The molecular ion CH<sup>+</sup> is not subject to chemical fractionation because it must be formed at high effective temperatures. The production of CH<sup>+</sup> is

<sup>1</sup> Based in part on observations made with the Very Large Telescope of the European Southern Observatory, Paranal, Chile, under programs 065.I-0526, 071.C-0367, 071.C-0513, and 076.C-0431.

<sup>2</sup> Department of Physics and Astronomy, University of Toledo, Toledo, OH 43606; adam.ritchey@utoledo.edu; steven.federman@utoledo.edu.

<sup>3</sup> Guest Observer, McDonald Observatory, University of Texas at Austin, Austin, TX 78712.

<sup>4</sup> W. J. McDonald Observatory, University of Texas at Austin, Austin, TX 78712; dll@astro.as.utexas.edu.

linked to the endothermic reaction  $C^+ + H_2 \rightarrow CH^+ + H$  (Elitzur & Watson 1978, 1980), which has an activation energy of  $\Delta E/k_B = 4640$  K. Since  $CH^+$  is associated with cold diffuse clouds, its formation requires that nonthermal processes, such as magnetohydrodynamic shocks or propagating Alfvén waves, provide the additional heating. As a result, the  $^{12}CH^+/^{13}CH^+$  ratio is believed to be equilibrated and thus to be the best measure of the ambient carbon isotopic ratio in the diffuse ISM. Many observations (e.g., Centurión & Vladilo 1991; Crane et al. 1991; Stahl & Wilson 1992; Centurión et al. 1995) have confirmed this expectation for  $CH^+$ , revealing  $^{12}CH^+/^{13}CH^+$  ratios very near 70 for local diffuse clouds. Centurión et al. (1995) give a weighted mean value of  $^{12}CH^+/^{13}CH^+$  of  $67 \pm 3$  for five sight lines to stars within approximately 500 pc of the Sun. However, some authors (e.g., Hawkins & Jura 1987; Vladilo et al. 1993; Casassus et al. 2005; Stahl et al. 2008) have reported discrepant values of  $^{12}CH^+/^{13}CH^+$ . Vladilo et al. (1993) found ratios of  $126 \pm 29$  and  $98 \pm 19$  toward HD 152235 and HD 152424, respectively. Since both of these stars belong to the Sco OB1 association (at  $d \simeq 2$  kpc), Vladilo et al. (1993) suggest that  $^{12}CH^+/^{13}CH^+$  may vary on scales of  $\sim 1$  kpc or smaller, depending on the distance to the clouds. Hawkins & Jura (1987) found  $^{12}CH^+/^{13}CH^+$  ratios of  $40 \pm 9$  and  $41 \pm 9$  toward 20 Tau and 23 Tau, respectively. Because these stars are members of the nearby Pleiades cluster ( $d = 110$  pc), such small values of  $^{12}CH^+/^{13}CH^+$  seem to challenge the view that a ratio near 70 characterizes the solar neighborhood.

Carbon-bearing molecules susceptible to fractionation, especially CO, may exhibit  $^{12}C$ -to- $^{13}C$  ratios that are either enhanced or reduced with respect to the ambient value. Two competing processes are capable of altering the  $^{12}CO/^{13}CO$  ratio in diffuse molecular gas. Selective photodissociation (SPD) favors  $^{12}CO$  since it is the more abundant isotopologue and is thus protected to a greater extent via self shielding (e.g., van Dishoeck & Black 1988; Visser et al. 2009). The process is effective in the case of CO because the photodissociation of this molecule is governed by line absorption. At lower gas kinetic temperatures, CO is influenced by the isotopic charge exchange (ICE) reaction  $^{13}C^+ + ^{12}CO \rightarrow ^{12}C^+ + ^{13}CO + \Delta E$ , where the difference in zero-point energies  $\Delta E/k_B = 35$  K (Watson et al. 1976) favors  $^{13}CO$ . Because CO is the most abundant carbon-bearing molecule in the ISM, an enhancement in  $^{13}CO$ , resulting from isotopic charge exchange, will deplete the carbon reservoir of  $^{13}C$ . Conversely, if  $^{13}CO$  is selectively destroyed through photodissociation, then the carbon reservoir will be enhanced in  $^{13}C$ . Any molecule arising from the remaining carbon in the reservoir should therefore possess a  $^{12}C$ -to- $^{13}C$  ratio that is fractionated in the opposite sense compared to the ratio in CO. Such behavior is expected for CN because this molecule coexists with CO in diffuse molecular clouds (Pan et al. 2005). Existing data on isotopologic ratios in CO, CN, and  $CH^+$  for the well-studied sight line to  $\zeta$  Oph offer some evidence that the chemical predictions are borne out. The diffuse gas in this direction has  $^{12}CO/^{13}CO = 167 \pm 15$  (Lambert et al. 1994),  $^{12}CN/^{13}CN = 47.3^{+5.5}_{-4.4}$  (Crane & Hegyi 1988), and  $^{12}CH^+/^{13}CH^+ = 67.5 \pm 4.5$  (Crane et al. 1991). Thus, the ratios in CO and CN are fractionated in opposing directions, while the ratio

in  $CH^+$  is consistent with the presumed ambient carbon isotopic ratio.

In this investigation, we seek to measure  $^{12}CN/^{13}CN$  and  $^{12}CH^+/^{13}CH^+$  ratios along lines of sight where  $^{12}CO/^{13}CO$  is either enhanced or reduced. Recent UV surveys of  $^{12}CO/^{13}CO$  along diffuse and translucent sight lines (Sonnentrucker et al. 2007; Burgh et al. 2007; Sheffer et al. 2007) have typically yielded ratios consistent with the average value of  $^{12}C/^{13}C$  for local interstellar clouds. Indeed, the weighted mean value of  $^{12}CO/^{13}CO$  for the 25 sight lines studied by Sheffer et al. (2007) is  $70 \pm 2$ . However, there are some notable exceptions. Enhanced ratios are found, not only in the direction of  $\zeta$  Oph, but also toward  $\rho$  Oph A and  $\chi$  Oph, where the respective  $^{12}CO/^{13}CO$  ratios are  $125 \pm 23$  and  $117 \pm 35$  (Federman et al. 2003), as well as toward  $\zeta$  Per, where  $^{12}CO/^{13}CO = 108 \pm 5$  (Sheffer et al. 2007). Reduced ratios, with respect to the ambient value, are found in the directions of 20 Aql, where  $^{12}CO/^{13}CO = 50 \pm 15$  (Hanson et al. 1992), and HD 154368, where  $^{12}CO/^{13}CO = 37 \pm 8$  (Sheffer et al. 2007), among several others (see Sheffer et al. 2007). Sonnentrucker et al. (2007) find a low  $^{12}CO/^{13}CO$  ratio toward HD 73882 ( $25 \pm 22$ ), but the relative uncertainties are large. Our goal is to obtain  $^{12}CN/^{13}CN$  and  $^{12}CH^+/^{13}CH^+$  ratios for as many of these sight lines as possible, so that, when our results are combined with the existing data on  $^{12}CO/^{13}CO$ , the suite of measurements can be used to test the predictions of chemical models for diffuse clouds. We reexamine the sight line to  $\zeta$  Oph as a check on our general methodology. We also obtain  $^{12}CH^+/^{13}CH^+$  ratios toward the Pleiades stars, 20 Tau and 23 Tau, to investigate potential scatter in the carbon isotopic ratio within the solar neighborhood.

Since high-quality data are needed to detect the weak features associated with  $^{13}CN$  and  $^{13}CH^+$ , the observations examined here also allow precise determinations of rotational excitation temperatures in CN. In some situations, these measurements can then be used to constrain the electron density, an important parameter for modeling the physical conditions within a given cloud (e.g., Black & van Dishoeck 1991). It is widely understood that the CN molecule is maintained in radiative equilibrium with the cosmic microwave background (CMB) in interstellar space (see the review by Thaddeus 1972). The CMB is the primary source of radiation in the universe at 2.64 mm and 1.32 mm, the wavelengths of the two lowest rotational transitions in CN. As a result, CN excitation temperatures reflect the temperature of the CMB at these wavelengths, in the absence of any local sources of excitation. Observed excitation temperatures in CN, in fact, do exhibit an excess over the temperature of the CMB, as derived from the Far Infrared Absolute Spectrophotometer (FIRAS) onboard the *COBE* satellite ( $T_{CMB} = 2.725 \pm 0.002$  K; Mather et al. 1999; see also Fixsen 2009), but this excess is small ( $< 0.1$  K; e.g., Palazzi et al. 1992). Since electron impact should dominate any local contribution to CN excitation (Thaddeus 1972), an observed excess provides an estimate for the density of electrons in the portion of the cloud traced by CN.

In order to investigate isotopologic ratios in CN and  $CH^+$  and CN rotational excitation in diffuse molecular clouds, we examine high-resolution, very high signal-to-

noise ratio observations of optical absorption lines arising from electronic transitions within the CN  $B^2\Sigma^+ - X^2\Sigma^+$  and CH<sup>+</sup>  $A^1\Pi - X^1\Sigma^+$  systems. The observations and data reduction procedures are described in § 2. In § 3, we provide detailed information concerning the profile synthesis routine, with which we derive our final column densities and isotopologic ratios. The analysis and discussion of our results on  $^{12}\text{CH}^+ / ^{13}\text{CH}^+$  and  $^{12}\text{CN} / ^{13}\text{CN}$  ratios appears in §§ 4.1 and 4.2, respectively. In § 4.3, we explore the relationship between  $^{12}\text{CN} / ^{13}\text{CN}$  and  $^{12}\text{CO} / ^{13}\text{CO}$  in an effort to evaluate the effects of chemical fractionation in diffuse molecular gas. The topic of CN rotational excitation is examined in § 5, and our main findings are summarized in § 6. An appendix gives results on weak Ca I and Ca II absorption toward  $\alpha$  Leo and  $\alpha$  Vir, which were observed as unreddened standard stars to aid in the reduction of the McDonald Observatory data (see § 2.1).

## 2. OBSERVATIONS AND DATA REDUCTION

### 2.1. McDonald Observatory Spectra

Principal data for this project were acquired with the Harlan J. Smith 2.7 m telescope at McDonald Observatory using the Tull (2dcoudé) spectrograph (Tull et al. 1995) in its high-resolution mode (cs21). The observations were carried out over the course of four observing runs between 2007 January and 2008 May. Two winter runs (2007 January and 2007 December/2008 January) provided data on 20 Tau, 23 Tau, and  $\zeta$  Per, while spectra of  $\rho$  Oph A,  $\zeta$  Oph, and 20 Aql were acquired during two summer observing sessions (2007 June and 2008 May). For all of the observations, the crossed-dispersed echelle spectrometer was configured with the 79 gr mm<sup>-1</sup> grating (E1), the 145  $\mu\text{m}$  slit (Slit 2), and a 2048  $\times$  2048 CCD (TK3). Order 56 of the E1 grating spectrum was centered at 4077 Å, enabling both the CN  $B-X$  (0, 0) lines near 3874 Å and the CH<sup>+</sup>  $A-X$  (0, 0) transition at 4232 Å to be recorded with a single exposure<sup>5</sup>. The grating tilt was adjusted slightly each night so that the interstellar features would not always fall on the same portion of the CCD. This helps to mitigate the effect of fixed pattern noise and reduces the chance that an instrumental glitch at a specific location on the CCD will negatively impact the observations.

The detection of absorption from the  $^{13}\text{C}$ -bearing isotopologues of CN and CH<sup>+</sup> requires spectra with very high signal-to-noise ratios ( $S/N > 1000$  per resolution element). To achieve this, the program stars were observed for several hours each night. Individual stellar exposures, taken in succession, were limited to 30 minutes to minimize the number of cosmic ray hits in each integration. A bright, unreddened star was observed nightly to the same signal level as the program stars to confirm that no instrumental defects were present at the locations of interstellar features. For both of the winter observing runs,  $\alpha$  Leo (Regulus; B7 V;  $B = 1.24$ ) served as the unreddened standard star. For the summer observations, either  $\alpha$  Vir (Spica; B1 III-IV+;  $B = 0.91$ ) or, on one occasion,  $\alpha$  Lyr (Vega; A0 V;  $B = 0.03$ ) was observed for this purpose. Calibration exposures for dark current and

bias correction, flat fielding, and wavelength assignment were obtained during each of the observing runs. Four 30-minute dark frames were acquired on the first night of a run, while a series of ten biases and ten flats were taken each night. For accurate wavelength calibration, Th-Ar comparison spectra were recorded throughout the night at intervals of 2–3 hr.

Reduction of the raw McDonald data employed standard routines within the Image Reduction and Analysis Facility (IRAF) environment. First, the overscan region in each of the raw images was fitted with a low-order polynomial and the excess counts were removed from the exposure. An average bias was created for each night and was used to correct the darks, flats, stellar exposures, and comparison lamp frames. No dark correction was applied to any of the observations because the level of dark current was always found to be insignificant after the bias was removed. Cosmic rays were eliminated from the stellar and comparison lamp exposures by setting the respective thresholds for detection to 50 and 25 times the mean of the surrounding pixels. Any cosmic rays present in individual flat lamp exposures were effectively removed by taking the median of all flats for a given night. Scattered light was modeled in the dispersion and cross-dispersion directions and subtracted from the stellar exposures and from the median flat. The flat was then normalized to unity and divided into the stellar and comparison lamp frames to account for (first-order) pixel-to-pixel variations across the CCD. One-dimensional spectra were extracted from the processed images by summing across the width of each order without weighting the individual pixels.

At this point, the extracted spectra of the program stars were examined in pixel space to determine the pixel coordinates of the interstellar absorption lines. The combined spectrum of the unreddened star from each night was then inspected at these positions to determine whether any instrumental defects remained after flat fielding. No obvious glitches were found in the vicinity of CN or CH<sup>+</sup>. However, low level fixed pattern noise was identified in some of the stellar spectra, particularly those with the highest S/N. To correct for these second-order fluctuations, the affected stellar exposures were divided by the normalized spectrum of the unreddened star for that night. The same technique, when applied to exposures with lower S/N, did not significantly improve the quality of the data and so was not adopted for these exposures. Next, stellar spectra were calibrated in wavelength after identifying emission lines in the Th-Ar comparison spectra, typically 5 per order. The dispersion solution applied to a given stellar exposure resulted from an interpolation between the solutions derived from the Th-Ar lamp exposures that preceded and followed the stellar exposure. Finally, the calibrated spectra were shifted to the reference frame of the local standard of rest (LSR).

All exposures of a given target from the multiple observing runs were coadded to maximize the S/N in the final spectrum. Before inclusion in the sum, each exposure was carefully examined, specifically near the expected positions of the  $^{13}\text{CN}$  and  $^{13}\text{CH}^+$  absorption features, to determine if any weak cosmic rays had survived the reduction process. When cosmic rays were identified, they were removed manually if they occurred far enough away from the interstellar features. If the cosmic

<sup>5</sup> This setting also provides data on the CH  $A-X$  (0, 0) transition at 4300 Å and on the Ca I  $\lambda 4226$  and Ca II  $\lambda 3933$  lines.

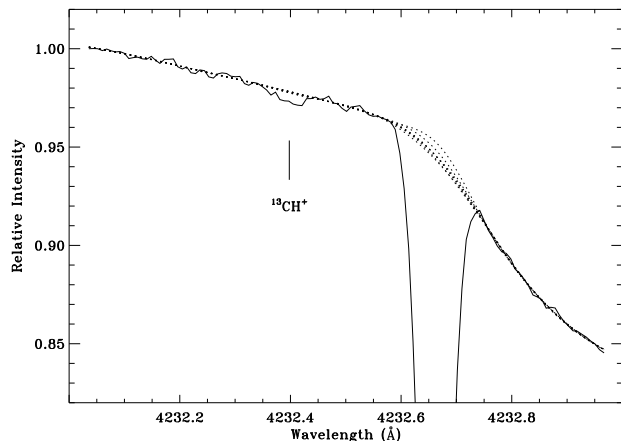


**Figure 1.** Possible continuum fits (*dotted lines*) to the region surrounding the  $\text{CH}^+$  lines toward 20 Tau. The strong interstellar  $^{12}\text{CH}^+$  line is superimposed on the blue wing of a photospheric Fe II line, complicating the placement of the continuum. The position of the  $^{13}\text{CH}^+$  line is indicated by a tick mark.

ray affected an interstellar feature directly, then the exposure was removed from the sum. Because the CN and  $\text{CH}^+$  lines reside in different echelle orders and the orders were coadded separately, an exposure removed from the sum in one order would not necessarily be removed in the other. Thus, the total exposure times for the two spectral regions may differ somewhat (see Table 1). Further complicating the coaddition process was a slight change in the resolving power of the spectrograph from one run to the next. The measured widths of thorium emission lines in the Th-Ar comparison spectra indicate a resolving power of  $R = 173,000$  ( $\Delta v = 1.7 \text{ km s}^{-1}$ ) was achieved during our run in 2007 January. This decreased to 150,000 ( $2.0 \text{ km s}^{-1}$ ) for the run in June of that year, but returned to 160,000 ( $1.9 \text{ km s}^{-1}$ ) and 168,000 ( $1.8 \text{ km s}^{-1}$ ) for the runs in 2007 December and 2008 May, respectively. When combining exposures from multiple observing runs, the data were sampled at the dispersion of the lowest resolution spectra contributing to the sum.

Final coadded spectra were normalized to the continuum by fitting low-order polynomials to regions free of interstellar absorption within a narrow spectral window (no more than  $2 \text{ \AA}$  wide) surrounding a given interstellar line. The immediate vicinity of the CN and  $\text{CH}^+$  lines in our McDonald spectra are free of contamination by either telluric or instrumental features, making continuum normalization straightforward. In only one case did the placement of the continuum present any significant difficulties. The interstellar  $^{12}\text{CH}^+$  line toward 20 Tau is superimposed onto a narrow photospheric Fe II feature at  $4233 \text{ \AA}$ . This situation is unique among the McDonald targets to 20 Tau, which has a relatively late spectral type and a rather slow rotation rate ( $v \sin i = 39 \text{ km s}^{-1}$ ; Hoffleit & Jaschek 1982). Figure 1 shows a range of possible continuum fits to the regions surrounding the  $\text{CH}^+$  lines toward 20 Tau. The small variation in the continuum above the  $^{13}\text{CH}^+$  feature at  $4232.4 \text{ \AA}$  has the greatest impact on the resulting  $^{12}\text{CH}^+ / ^{13}\text{CH}^+$  ratio, but this variation is less than 10% of the  $^{13}\text{CH}^+$  line strength, which is well within the 20% observational errors associated with the detection of this weak feature.

## 2.2. VLT/UVES Archival Spectra

To supplement our high signal-to-noise McDonald observations of bright targets, optical spectra of seven fainter stars were obtained from the European Southern Observatory (ESO) Science Archive Facility. These spectra were acquired by the Ultraviolet and Visual Echelle Spectrograph (UVES) of the Very Large Telescope (VLT) at Cerro Paranal, Chile primarily during two observing programs designed to measure  $^{12}\text{CH}^+ / ^{13}\text{CH}^+$  ratios (see Casassus et al. 2005; Stahl et al. 2008). The primary UVES data (from programs 071.C-0367 and 076.C-0431; S. Casassus, PI) have S/N ratios that are comparable to those of our McDonald spectra. These observations employed the central wavelength setting at  $4370 \text{ \AA}$ , which allows continuous spectral coverage from  $3750\text{--}5000 \text{ \AA}$ , a range that includes the CN (0, 0),  $\text{CH}^+$  (0, 0), and  $\text{CH}^+$  (1, 0) lines. Other VLT/UVES datasets were obtained (from program 065.I-0526; E. Roueff, PI) that were acquired using the wavelength setting at  $3460 \text{ \AA}$ . This setting covers the region from  $3050\text{--}3870 \text{ \AA}$  and permits detection of the CN (1, 0) lines near  $3579 \text{ \AA}$ . The observations at  $3460 \text{ \AA}$  typically have lower S/N than those at  $4370 \text{ \AA}$ . For one sight line (HD 210121), observations at  $3460 \text{ \AA}$  and  $4370 \text{ \AA}$  were provided by program 065.I-0526 and additional data acquired with the wavelength setting at  $3900 \text{ \AA}$  were obtained from program 071.C-0513 (M. André, PI).

The weaker CN and  $\text{CH}^+$  (1, 0) lines provide a check on the column densities derived from the stronger (0, 0) lines, which is especially important when the (0, 0) lines become optically thick. The seven UVES sight lines chosen for this study (see Table 1) are known from previous observations (e.g., Gredel et al. 1991; Palazzi et al. 1992) to have strong lines of interstellar CN and determining  $^{12}\text{CN} / ^{13}\text{CN}$  ratios will be our focus. We do not rederive  $^{12}\text{CH}^+ / ^{13}\text{CH}^+$  ratios for the UVES sight lines as there are significant uncertainties associated with such determinations from these data (see § 3). While the principal reason for incorporating the UVES spectra into our analysis was to expand our sample to include more heavily-reddened sight lines, the VLT observing programs also provided us with additional data on some of our McDonald targets. Both 23 Tau and  $\zeta$  Oph were observed at  $4370 \text{ \AA}$  under programs 076.C-0431 and 071.C-0367, respectively, and observations of  $\rho$  Oph A and  $\zeta$  Oph at  $3460 \text{ \AA}$  are available from program 065.I-0526. These supplementary data are useful for making comparisons with our McDonald results.

All VLT/UVES datasets were reduced with the UVES pipeline software in optimal extraction mode unless the observations employed an image slicer in which case the average extraction method had to be adopted. Master bias and master flat frames were created for each night for which we obtained science observations. Th-Ar lamp spectra acquired contemporaneously with the science data were used for wavelength calibration. After extraction, all echelle orders from a given exposure were merged and the resulting spectra were shifted to the LSR frame of reference. Finally, all individual exposures of the same target obtained with the same instrumental setup were coadded. The spectral resolution of the UVES data varies somewhat for the different observing programs due to changes in slit width and CCD binning.

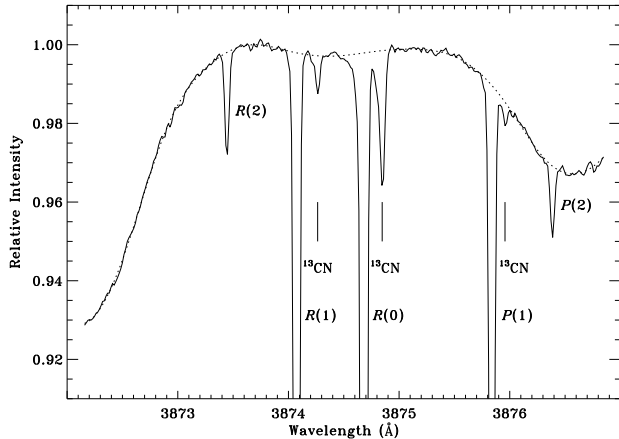


**Figure 2.** Coadded UVES spectrum of CN  $B-X$  (0, 0) toward HD 169454 showing the adopted continuum fit (*dotted line*). Each line is labeled and the positions of the  $R(0)$ ,  $R(1)$ , and  $P(1)$  lines of  $^{12}\text{CN}$  are indicated by tick marks. This is the first reported detection of the  $^{13}\text{CN}$   $P(1)$  line in the interstellar medium. Note also that absorption from  $^{13}\text{CN}$   $R(0)$  is partially blended with the much stronger  $^{12}\text{CN}$   $R(0)$  line.

The primary data at 4370 Å have a velocity resolution of  $\Delta v = 3.5 \text{ km s}^{-1}$ , corresponding to a resolving power of  $R = 85,000$ . The observations at 3460 Å employed either  $1 \times 1$  or  $1 \times 2$  binning and have resolutions of  $3.8 \text{ km s}^{-1}$  ( $R = 79,000$ ) or  $4.2 \text{ km s}^{-1}$  ( $R = 71,000$ ), respectively. For HD 210121, the observations at 4370 Å were combined with those at 3900 Å in the overlapping region, and the resulting spectrum has a resolution corresponding to  $R = 80,000$ .

The coadded UVES spectra in the vicinity of CN were normalized to the continuum in much the same way as were the McDonald data except that a larger spectral window was used (typically 5 Å) that included all of the lines of the CN (0, 0) or (1, 0) band. The  $R(0)$  and  $R(1)$  lines in these data are separated by very little continuum due to the lower resolution. The larger spectral windows, in addition to a non-negligible amount of residual fringing in the extracted spectra, meant that higher-order polynomials had to be applied during the normalization process. Moreover, the  $^{12}\text{CN}$  and  $^{13}\text{CN}$   $R(0)$  lines of the (0, 0) band, which are separated by approximately  $13.5 \text{ km s}^{-1}$ , are partially blended in the UVES spectra, again a result of the coarse resolution but also due to the strength of CN absorption along these lines of sight. Absorption from  $^{13}\text{CN}$  is thus found on the redward wing of the  $^{12}\text{CN}$  line (as shown in Figure 2), adding some uncertainty to the placement of the continuum in this region. The situation is not as problematic as in the case of  $\text{CH}^+$  from these data, however, because the CN lines are intrinsically narrow and exhibit mostly single velocity components.

### 2.3. Stellar Sample and Observational Results

The total exposure times and signal-to-noise ratios per resolution element achieved for each of the McDonald and UVES targets are shown in Table 1 along with the relevant stellar data, consisting of the spectral type,  $B$  magnitude,  $E(B - V)$  color excess, Galactic  $l$  and  $b$  coordinates, and distance. We list the *Hipparcos* parallax distance (Perryman et al. 1997) if the measurement is significant at the  $4\text{-}\sigma$  level or greater. Otherwise, the dis-

tance we derive from the method of spectroscopic parallax is given. The spectral types in Table 1 are from the same references that provided values of  $E(B - V)$ , although, for HD 73882, HD 154368, and HD 170740, the spectral types were actually listed in a previous paper by the same group (Rachford et al. 2002). From these references, we also obtained the  $V$  magnitude and total visual extinction ( $A_V$ ) for each star without a precise *Hipparcos* measurement so that spectroscopic distances could be derived using a self-consistent set of photometric data. As the distances in Table 1 indicate, our selection of interstellar sight lines samples almost exclusively the local ISM. Only four stars in the sample (HD 73882, HD 152236, HD 154368, and HD 169454) lie farther than 500 pc from the Sun. Accordingly, these stars also exhibit the highest degrees of interstellar reddening, with the largest value of  $E(B - V)$  found in the direction of HD 169454. Even along the more extended sight lines, however, the clouds responsible for CN and  $\text{CH}^+$  absorption are likely to be nearby. This can be deduced from the velocities of the molecular components, which correspond to the dominant components in species like Ca II. The more distant stars have rather more complicated profiles of Ca II  $\lambda 3933$ , but the dominant components are always found near  $v_{\text{LSR}} = 0 \text{ km s}^{-1}$ , implying that the absorption originates in local gas.

The S/N ratios in Table 1 result in uncertainties in equivalent width ( $W_\lambda$ ) of 0.06 mÅ, on average, for the CN and  $\text{CH}^+$  lines in our McDonald spectra. For the primary UVES data, the average uncertainty in  $W_\lambda(\text{CN})$  is 0.05 mÅ. Despite the small uncertainties, we do not detect absorption from  $^{13}\text{CH}^+$  toward  $\zeta$  Per or 20 Aql, which is not unexpected considering the weak  $^{12}\text{CH}^+$  lines in these directions. The  $3\text{-}\sigma$  upper limits on the equivalent widths of  $^{13}\text{CH}^+$  are  $\lesssim 0.18 \text{ mÅ}$  for  $\zeta$  Per and  $\lesssim 0.24 \text{ mÅ}$  for 20 Aql. We also do not detect any CN absorption from either isotopologue in the directions of 20 Tau and 23 Tau, but obtain upper limits on  $W_\lambda(^{12}\text{CN})$  of  $\lesssim 0.25 \text{ mÅ}$  and  $\lesssim 0.13 \text{ mÅ}$  for the two sight lines, respectively. The equivalent widths for detected lines are given in Table 2 for  $\text{CH}^+ \lambda 4232$  and Table 3 for CN  $\lambda 3874$ . We list the fitted equivalent widths that result from our profile synthesis analysis (see § 3). Uncertainties in  $W_\lambda$  were calculated as the product of the rms variations in the continuum and the full width at half maximum (FWHM) in the line<sup>6</sup>. Note the quite strong detections of  $^{13}\text{CN}$  toward the UVES targets. While not listed in Table 3, the weak  $R(2)$  and  $P(2)$  lines of  $^{12}\text{CN}$  are detected toward most of the stars in our sample with CN absorption. In our McDonald spectra, however, these features are only marginal. For  $\zeta$  Oph and HD 152236,

<sup>6</sup> While we do not formally include continuum placement errors when calculating uncertainties in  $W_\lambda$ , the uncertainties derived using our method are more conservative than those based on statistical errors (adopting the formula given in Jenkins et al. 1973) and our estimates for continuum placement errors added in quadrature. As an example, the statistical error in the equivalent width of the  $^{13}\text{CH}^+$  line toward 20 Tau is  $\sigma_{W,\text{rms}} = (\Delta\lambda)(N_p^{1/2})(\text{rms}) = 0.0496 \text{ mÅ}$ , where  $\Delta\lambda = 0.00802 \text{ Å}$  is the wavelength dispersion,  $N_p = 21$  is the number of pixels sampling the line profile, and  $\text{rms} = 0.00135$  is the root mean square of the noise in the continuum. The standard deviation in the measured value of  $W_\lambda(^{13}\text{CH}^+)$  for a range of possible continuum fits (see Figure 1) is  $\sigma_{W,\text{cont}} = 0.0229 \text{ mÅ}$ . Thus, the total error would be  $\sigma_W = (\sigma_{W,\text{rms}}^2 + \sigma_{W,\text{cont}}^2)^{1/2} = 0.0546 \text{ mÅ}$ , while our method gives  $\sigma_W = (\text{FWHM})(\text{rms}) = 0.0730 \text{ mÅ}$ .

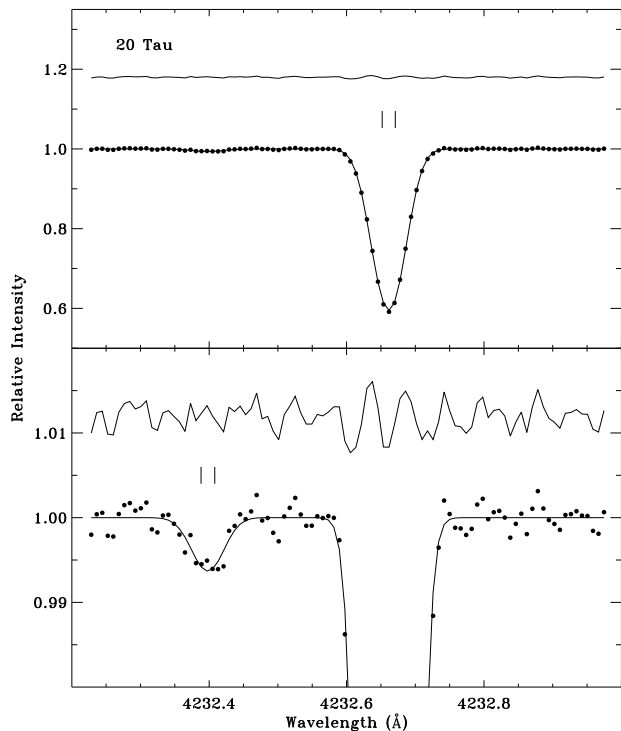


**Figure 3.** Simultaneous profile synthesis fit to the  $^{12}\text{CH}^+$  and  $^{13}\text{CH}^+$   $R(0)$  lines toward 20 Tau scaled to show the stronger (*upper panel*) and weaker (*lower panel*) isotopologue. The synthetic profile is shown as a solid line passing through data points that represent the observed spectrum. Residuals are plotted above the fit. Individual velocity components are indicated by tick marks.

the lower signal-to-noise ratios near  $3874 \text{ \AA}$ , compared to other stars observed with the same instrument, prevent any detection of  $R(2)$  or  $P(2)$ . Remarkably, four of the UVES targets exhibit fairly significant absorption from  $^{13}\text{CN } R(1)$ , and in the spectrum of HD 169454, the  $^{13}\text{CN } P(1)$  line is detected with a significance of  $8 \sigma$  (see Figure 2). Also shown in the tables are previous results from the literature on  $\text{CH}^+$  and  $\text{CN}$  toward our targets, where we have included only those studies that give equivalent widths for the weaker isotopologue or for the  $R(1)$  and  $P(1)$  lines in the case of  $\text{CN}$ . Studies that examined only the strongest line in  $\text{CH}^+$  or  $\text{CN}$  are omitted.

### 3. PROFILE SYNTHESIS

The  $\text{CN}$  and  $\text{CH}^+$  absorption profiles were synthesized with the rms-minimizing code ISMOD (Y. Sheffer, unpublished) that treats the velocities ( $v$ ), Doppler  $b$ -values, and column densities ( $N$ ) of the absorption components as free parameters. ISMOD assumes a Voigt profile function for each absorption component and convolves the intrinsic profile with an instrumental profile, represented by a Gaussian with a width determined by the resolving power of the instrument (see Black & van Dishoeck 1988). The  $R(0)$  lines of the  $(0, 0)$  bands in  $\text{CN}$  and  $\text{CH}^+$  were used to derive the  $N(^{12}\text{CN})/N(^{13}\text{CN})$  and  $N(^{12}\text{CH}^+)/N(^{13}\text{CH}^+)$  ratios. Both isotopologues of  $\text{CN}$  and of  $\text{CH}^+$  were fitted simultaneously by requiring the component structure of the two profiles to be identical. Thus, the 12-to-13 column density ratio and the isotope shift between the two lines were additional free parameters.

Figures 3 through 10 present the  $\text{CH}^+$  and  $\text{CN } R(0)$  fits

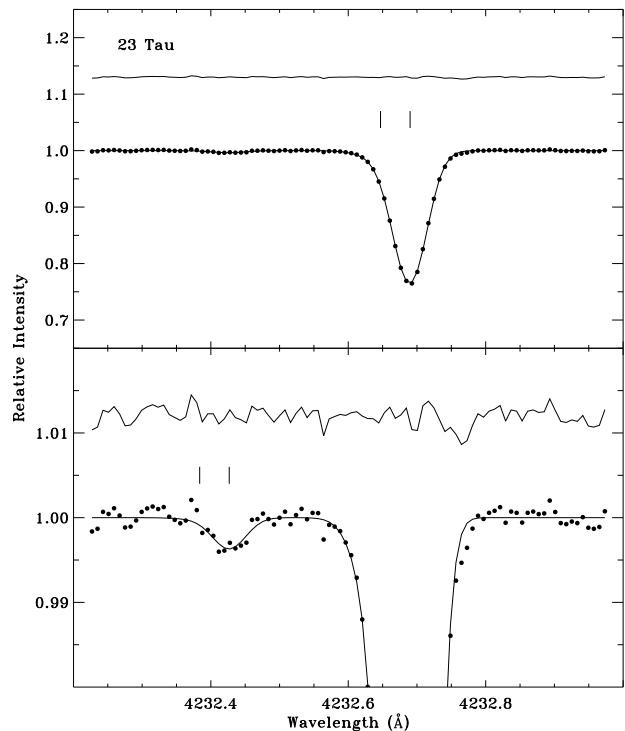


**Figure 4.** Same as Figure 3 except for the  $^{12}\text{CH}^+$  and  $^{13}\text{CH}^+$   $R(0)$  lines toward 23 Tau.

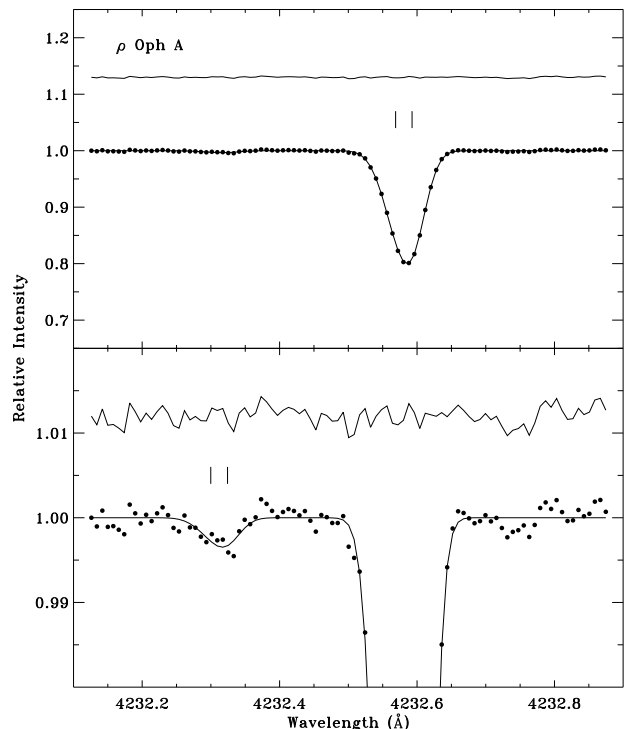


**Figure 5.** Same as Figure 3 except for the  $^{12}\text{CH}^+$  and  $^{13}\text{CH}^+$   $R(0)$  lines toward  $\rho$  Oph A.

for the data acquired at McDonald Observatory. When fitting the  $\text{CH}^+$  lines toward 20 Tau and 23 Tau, we used our previous results on the component structure in these directions (Ritchey et al. 2006) as the initial input to the profile synthesis routine. Likewise, the initial values for the component structure of  $\text{CH}^+$  toward  $\rho$  Oph A

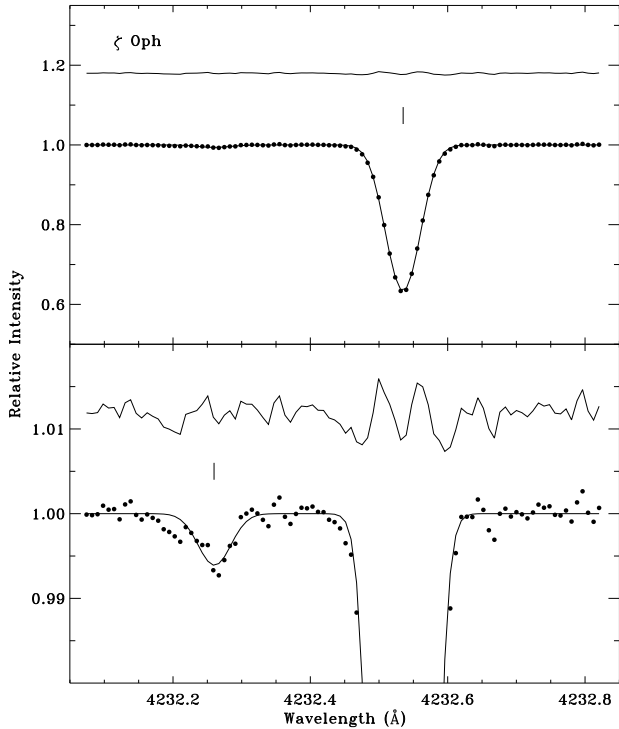


**Figure 6.** Same as Figure 3 except for the  $^{12}\text{CH}^+$  and  $^{13}\text{CH}^+$   $R(0)$  lines toward  $\zeta$  Oph.

were obtained from Pan et al. (2004). The input values for the CN  $R(0)$  line toward  $\zeta$  Oph were taken from the ultra-high resolution ( $R = 600,000$ ) study by Lambert et al. (1990), who modeled CN absorption along this sight line with two Gaussian components separated by  $1.2 \text{ km s}^{-1}$ . Because our study has coarser resolution and the component parameters in this case were already precisely determined, the velocity difference between the two components, their relative strengths, and their  $b$ -values were held fixed in our analysis. Lambert et al. (1990) also examined  $\text{CH}^+$  toward  $\zeta$  Oph, but modeled the line with a single Gaussian component. Absorption profiles with single components do not require precise input parameters in ISMOD. Thus, for the  $\text{CH}^+$  line toward  $\zeta$  Oph, as well as for the CN  $R(0)$  lines toward the other McDonald targets, input parameters were determined by direct examination of the spectra within IRAF. The velocities and column densities of the interstellar absorption components in our profile synthesis fits were computed using the wavelengths and oscillator strengths ( $f$ -values) presented in Table 4.

Among the optical tracers of diffuse molecular gas, the CN molecule typically probes the densest portion of a diffuse cloud (Pan et al. 2005). As a consequence, CN line widths are intrinsically small, corresponding to  $b$ -values that are less than  $1.0 \text{ km s}^{-1}$  in most cases. With such narrow lines, the strongest transitions in CN can become optically thick even at moderate column densities. While this is not a major concern for our McDonald sight lines, all of which have optical depths ( $\tau$ ) at line center that are less than 1.0, it is an important consideration for the UVES observations, where the average value of  $\tau$  for the (0, 0)  $R(0)$  line is 4.45. When large optical depths are present, a small change in  $b(\text{CN})$  will have a dramatic impact on the  $^{12}\text{CN}$  column density obtained from the

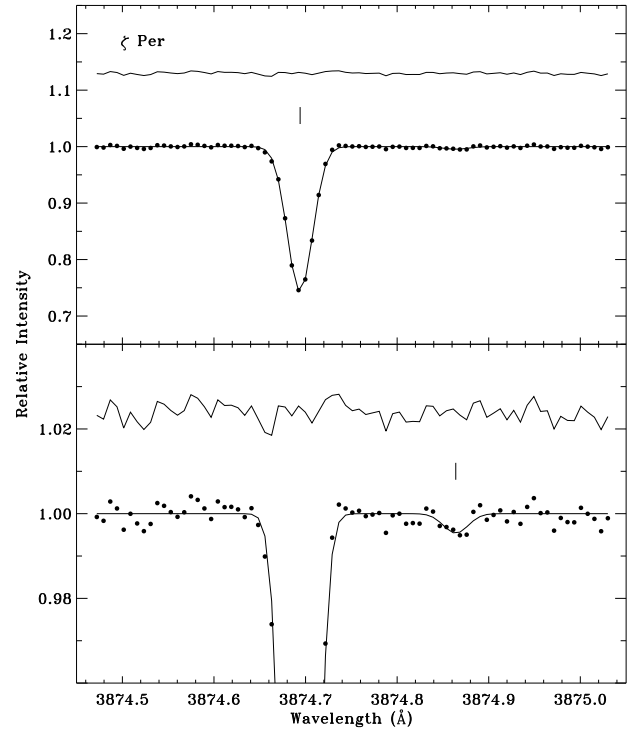


**Figure 7.** Simultaneous profile synthesis fit to the  $^{12}\text{CN}$  and  $^{13}\text{CN}$   $R(0)$  lines toward  $\zeta$  Per scaled to show the stronger (*upper panel*) and weaker (*lower panel*) isotopologue. Plotting symbols are the same as in Figure 3.

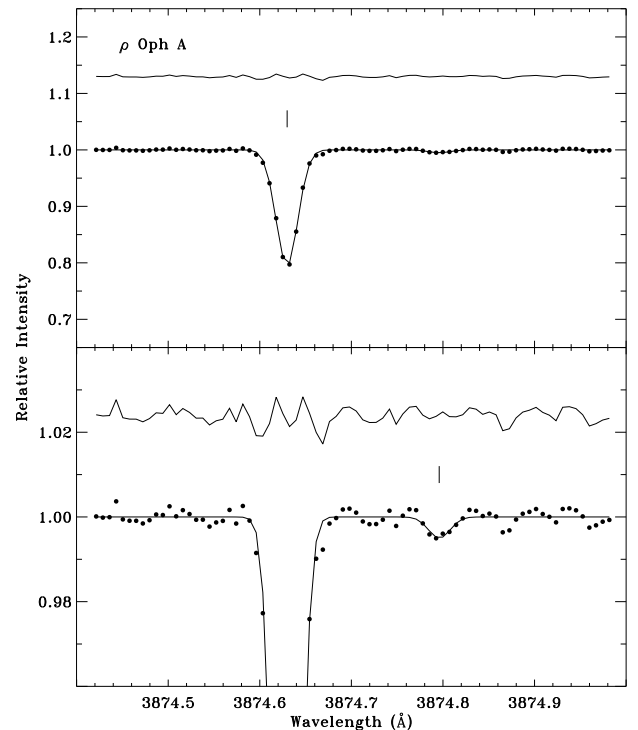


**Figure 8.** Same as Figure 7 except for the  $^{12}\text{CN}$  and  $^{13}\text{CN}$   $R(0)$  lines toward  $\rho$  Oph A.

strong  $R(0)$  line, and the resulting  $^{12}\text{CN}/^{13}\text{CN}$  ratio will be similarly affected. Moreover, because the UVES spectra are sampled at moderate resolution ( $\sim 3.5 \text{ km s}^{-1}$ ), the CN lines are dominated by instrumental rather than

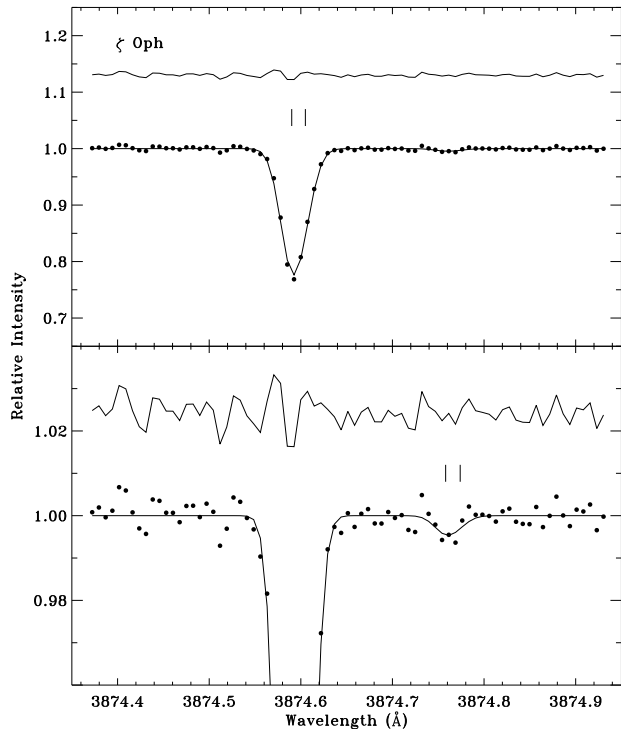


**Figure 9.** Same as Figure 7 except for the  $^{12}\text{CN}$  and  $^{13}\text{CN}$   $R(0)$  lines toward  $\zeta$  Oph.

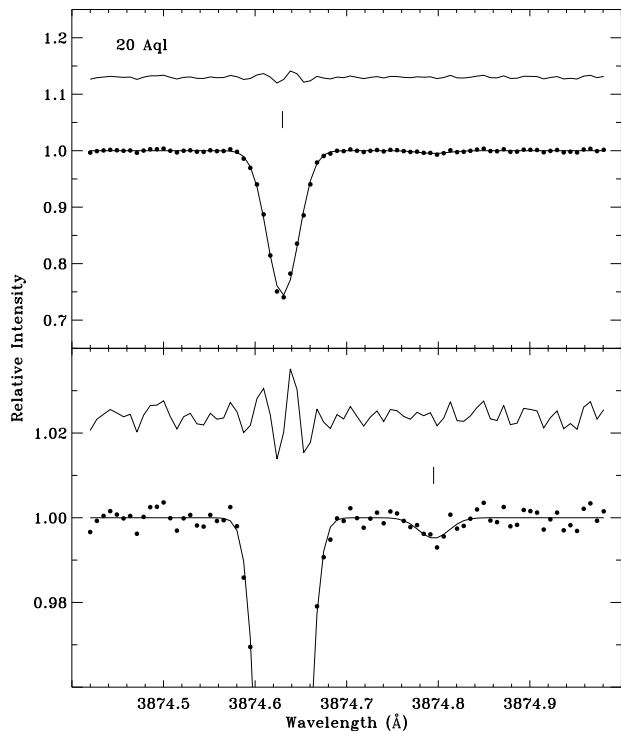


**Figure 10.** Same as Figure 7 except for the  $^{12}\text{CN}$  and  $^{13}\text{CN}$   $R(0)$  lines toward 20 Aql.

intrinsic broadening, making direct evaluation of the  $b$ -values more difficult. To minimize these uncertainties,  $b$ -values for optically thick lines were derived using the well-known doublet ratio method, which has often been employed in this context (e.g., Meyer & Jura 1985; Gredel et al. 1991; Roth & Meyer 1995). The method is

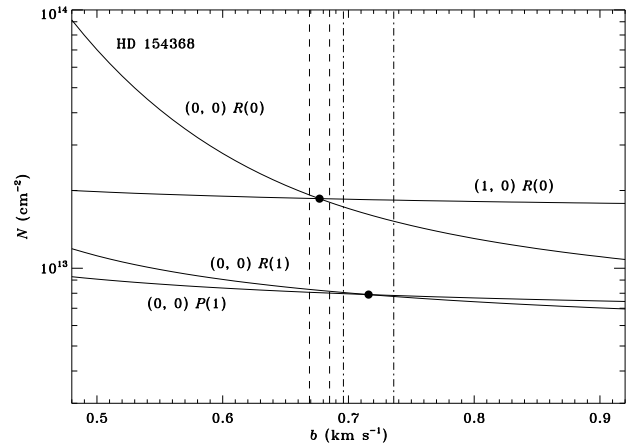


**Figure 11.** Column density as a function of  $b$ -value for the four CN transitions used to derive  $b$  in the main component toward HD 154368 via the doublet ratio method (see text). The intersection of each pair of curves, which gives the  $b$ -value corresponding to the measured doublet ratio, is marked by a solid point. The  $1\text{-}\sigma$  errors on  $b$  thus derived are shown as dashed lines for the  $(0, 0)/(1, 0)$   $R(0)$  pair and dot-dashed lines for the  $(0, 0) R(1)/P(1)$  pair.

predicated on the fact that two lines arising from the same state must yield identical column densities for some value of  $b$ . In the case of CN, one can use either the  $(0, 0)$   $R(1)$  and  $P(1)$  lines or the  $(0, 0)$  and  $(1, 0)$   $R(0)$  lines. Having observations of both pairs is advantageous as it allows independent checks on consistency.

In the optically thin limit, the equivalent width of an absorption line is proportional to the column density such that  $W_\lambda \propto \lambda^2 f N$  (see Spitzer 1978). Thus, for a pair of optically thin lines that must yield identical values of  $N$ , the equivalent width ratio is given by  $W_{\lambda,1}/W_{\lambda,2} = (\lambda_1/\lambda_2)^2 f_1/f_2$ . Specifically, from the molecular line parameters in Table 4, the  $(0, 0)$   $R(1)/P(1)$  equivalent width ratio for optically thin absorption is equal to 2.00, while the  $(0, 0)/(1, 0)$   $R(0)$  ratio is equal to 13.35. The measured ratio will be lower if the optical depth of the stronger line is significant. To derive  $b$ -values using this approach, the CN equivalent widths were determined by fitting simple Gaussians to the observed profiles within IRAF. Column densities based on the measured equivalent widths for a given pair of lines were then interpolated from a set of curves of growth calculated on the interval  $0.30 \leq b \leq 0.99 \text{ km s}^{-1}$  with a step size of  $0.01 \text{ km s}^{-1}$ . The result of this procedure was a pair of curves that give  $N$  as a function of  $b$  for the two transitions, corresponding to the measured values of  $W_\lambda$ . By plotting these curves and finding the intersection in the  $N$ - $b$  plane, one finds the unique  $b$ -value that yields identical column densities for the pair of lines (see Figure 11).

Table 5 gives the observed CN  $(0, 0) R(1)/P(1)$  equivalent width ratios, and  $(0, 0)/(1, 0) R(0)$  ratios if possible, for all of the stars in our sample where CN is detected. For the main CN component toward HD 152236, both ratios are consistent with the optically thin limit. The  $R(1)/P(1)$  ratio of  $1.91 \pm 0.10$  nominally gives a  $b$ -value of  $0.39 \text{ km s}^{-1}$ , but with an upper bound at infinity. An infinite  $b$ -value in this context means that the lines fall on the linear portion of the curve of growth and cannot be used to constrain the Doppler parameter. This is evidently the case for the CN lines toward our McDonald targets, which yield no definitive information on  $b$ . It is



worth noting, however, that the (0, 0)/(1, 0)  $R(0)$  equivalent width ratios toward  $\rho$  Oph A and  $\zeta$  Oph would result in  $b$ -values of  $0.60 \text{ km s}^{-1}$  and  $0.88 \text{ km s}^{-1}$ , respectively. Even if the uncertainties give infinite upper bounds, the nominal results are similar to the results of many earlier investigations. For instance, Palazzi et al. (1992) find  $b = 0.84 \pm 0.22 \text{ km s}^{-1}$  in the direction of  $\rho$  Oph A, while Pan et al. (2004) list a value of  $0.7 \text{ km s}^{-1}$ . For  $\zeta$  Oph, Crane et al. (1986) give  $b = 0.88 \pm 0.02 \text{ km s}^{-1}$ , and Roth & Meyer (1995) find  $b = 0.89 \pm 0.19 \text{ km s}^{-1}$ . The CN absorption profiles toward HD 161056 arise from two components of approximately equal strength, separated by  $5.9 \text{ km s}^{-1}$ . Interestingly, the  $R(1)/P(1)$  ratio for the component at  $-3.1 \text{ km s}^{-1}$  indicates that this component has a slightly larger optical depth than the component at  $+2.8 \text{ km s}^{-1}$ , although the (0, 0)/(1, 0)  $R(0)$  ratios in both cases exceed the optically thin limit.

The UVES sight lines in Table 5 other than HD 152236 and HD 161056 exhibit fairly significant optical depths in their CN absorption lines. An extreme case is presented by the sight line to HD 169454, for which the (0, 0)/(1, 0)  $R(0)$  equivalent width ratio is only  $2.83 \pm 0.05$ . Where measurements on both pairs of CN transitions are available, the derived  $b$ -values agree remarkably well. Note that the ratio between the (0, 0)  $R(0)$  and (1, 0)  $R(0)$  equivalent widths provides the most stringent constraints on  $b$  because of the larger difference in intrinsic line strength for this pair, compared to  $R(1)$  and  $P(1)$ . The weighted mean of the two  $b$ -values in the case of HD 154368 is  $b = 0.68 \pm 0.01 \text{ km s}^{-1}$ , while for HD 169454, HD 170740, and HD 210121 the weighted means are  $b = 0.50 \pm 0.01 \text{ km s}^{-1}$ ,  $b = 0.46 \pm 0.04 \text{ km s}^{-1}$ , and  $b = 0.80 \pm 0.02 \text{ km s}^{-1}$ , respectively. Palazzi et al. (1990) obtained a  $b$ -value of  $0.65 \pm 0.01 \text{ km s}^{-1}$  for HD 154368, and the study by Roth & Meyer (1995) resulted in a  $b$ -value of  $0.68 \pm 0.08 \text{ km s}^{-1}$  in this direction. Additionally, Palazzi et al. (1992) find  $b = 0.64 \pm 0.17 \text{ km s}^{-1}$  for HD 169454, and  $b = 0.84 \pm 0.20 \text{ km s}^{-1}$  for HD 170740. Sheffer et al. (2008) give the  $b$ -value toward HD 210121 as  $0.9 \text{ km s}^{-1}$ . These various determinations show good agreement, except in the case of HD 170740. Yet, even for this sight line, the discrepancy is not that severe. The Palazzi et al. (1992)  $b$ -value actually agrees with our more precise determination within  $2 \sigma$  and our result is particularly secure because it was derived from measurements of four different CN transitions across two distinct bands, which were observed independently. Indeed, as a result of the excellent agreement between  $b$ -values determined from the two equivalent width ratios, the weighted means for HD 154368, HD 169454, HD 170740, and HD 210121 were used as fixed input in the profile fitting analysis. For HD 73882, HD 152236, and HD 161056, the  $b$ -values obtained from the  $R(1)/P(1)$  ratios were used as the initial input to ISMOD but were allowed to vary.

The component parameters resulting from our profile synthesis fits to the CH<sup>+</sup> and CN  $R(0)$  lines of the (0, 0) bands are presented in Table 6. In cases where isotopologic ratios were determined (see Table 7), the quoted velocities and  $b$ -values apply to both the <sup>12</sup>C and <sup>13</sup>C-bearing isotopologues since the two profiles were required to have identical component structure. Uncertainties in  $N$  for a given component were derived from the relative uncertainties in  $\tilde{W}_\lambda$ . For 20 Tau and 23 Tau, the new

results are consistent with our previous analysis of CH<sup>+</sup> absorption in the Pleiades from McDonald spectra with much lower signal to noise (Ritchey et al. 2006). The only major difference is that, in the present investigation, we derive a 10% higher column density of <sup>12</sup>CH<sup>+</sup> toward 20 Tau, even though the equivalent widths agree to within 2%. As profile synthesis was not used previously to obtain column densities, the discrepancy underscores the importance of carefully considering optical depth effects when dealing with strong absorption lines. For 23 Tau, both the equivalent widths and column densities of <sup>12</sup>CH<sup>+</sup> from this and the previous study are consistent at the 1% level. Our new results on CH<sup>+</sup> toward  $\rho$  Oph A are also broadly consistent with the analysis of Pan et al. (2004), who give a total <sup>12</sup>CH<sup>+</sup> column density that differs from our value by less than 1%. In the case of CN toward  $\rho$  Oph A, our profile fit results in a  $b$ -value of  $0.4 \text{ km s}^{-1}$ , somewhat lower than the  $0.7 \text{ km s}^{-1}$  given by Pan et al. (2004). Since the equivalent width measurements are essentially identical, the difference in  $b$  amounts to a 20% increase in  $N(^{12}\text{CN})$  in the present analysis.

Table 7 lists the <sup>12</sup>CN/<sup>13</sup>CN and <sup>12</sup>CH<sup>+</sup>/<sup>13</sup>CH<sup>+</sup> column density ratios for our sample along with the isotope shifts and total molecular column densities derived through profile synthesis of the (0, 0) bands in CN and CH<sup>+</sup>. The uncertainties in <sup>12</sup>CN/<sup>13</sup>CN and <sup>12</sup>CH<sup>+</sup>/<sup>13</sup>CH<sup>+</sup> were obtained by propagating the errors associated with the column densities of the two isotopologues, although the errors in  $N$  for the weaker isotopologue essentially determine the outcome. Also included in Table 7 are column densities and 12-to-13 ratios for CO from the literature, where such measurements exist. In Table 8, we present a comparison between the column densities that we derive from the (0, 0)  $R(0)$  and (1, 0)  $R(0)$  lines of CH<sup>+</sup> and CN. The good agreement indicates that we have adequately accounted for optical depth effects in these spectra, giving us confidence in our isotopologic results.

As mentioned in § 2.2, we are not confident that <sup>12</sup>CH<sup>+</sup>/<sup>13</sup>CH<sup>+</sup> ratios can be reliably obtained for the UVES sight lines. A number of contributing factors lead us to this assessment. There is a non-negligible amount of fringing in the reduced UVES spectra, making an unambiguous placement of the continuum impossible. The problem is compounded by the broad and moderately complex CH<sup>+</sup> absorption profiles, which often consist of three or more components (see Table 6). Particularly worrisome are weak <sup>12</sup>CH<sup>+</sup> components that lie to the blue of the main component (for instance, toward HD 152236, HD 154368, and HD 169454). In the (0, 0) line at  $4232 \text{ \AA}$ , these components are likely to be blended with the strongest feature in <sup>13</sup>CH<sup>+</sup>, considering that the isotope shift is  $-19 \text{ km s}^{-1}$ . In principle, one could constrain the <sup>12</sup>CH<sup>+</sup> absorption profile using the (1, 0) transition at  $3957 \text{ \AA}$  since the <sup>13</sup>CH<sup>+</sup> line corresponding to this transition is shifted by  $33 \text{ km s}^{-1}$  to the red of <sup>12</sup>CH<sup>+</sup>, rather than to the blue. In practice, however, components that are already weak at  $4232 \text{ \AA}$  may not even be detected in the weaker transition at  $3957 \text{ \AA}$ , limiting the usefulness of this approach.

Ultimately, we did synthesize the CH<sup>+</sup> profiles toward the UVES targets in an attempt to derive <sup>12</sup>CH<sup>+</sup>/<sup>13</sup>CH<sup>+</sup> ratios, but the results bore out our initial concerns. No

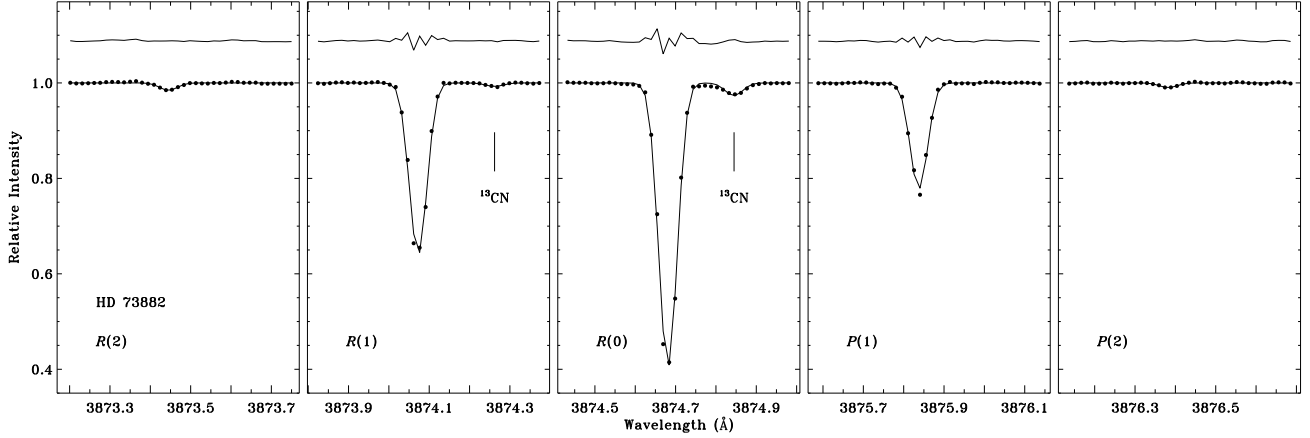


**Figure 12.** Profile synthesis fits to the  $B-X$  (0, 0) band of CN toward HD 73882. See Figure 3 for a description of the plotting symbols. The same range in velocity is shown for each panel. The positions of the  $R(0)$  and  $R(1)$  lines of  $^{13}\text{CN}$  are indicated by tick marks. When both isotopologues are present, the two profiles are synthesized simultaneously.

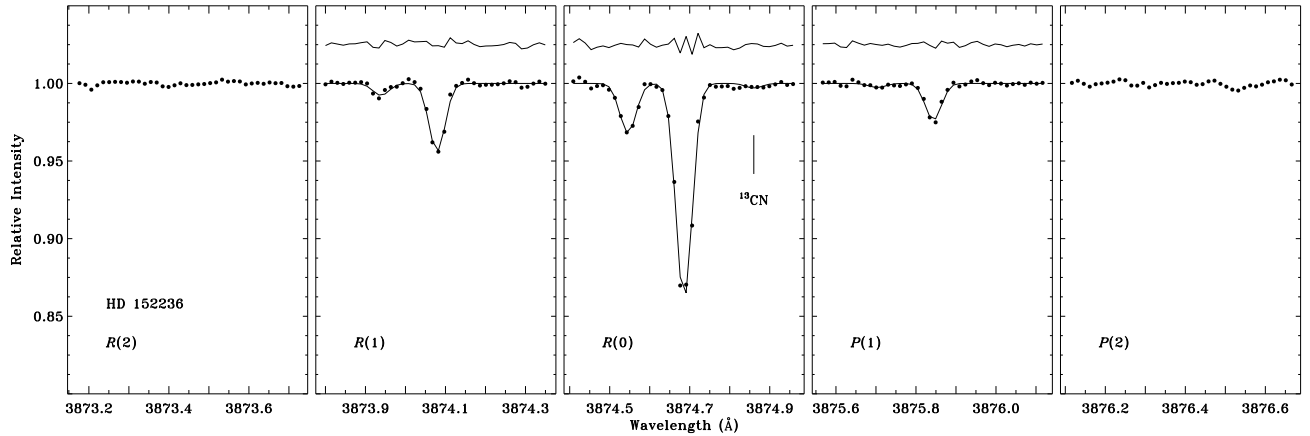


**Figure 13.** Same as Figure 12 except for the CN  $B-X$  (0, 0) band toward HD 152236. Two line-of-sight components are clearly identified in the  $R(0)$  and  $R(1)$  lines of  $^{12}\text{CN}$  and are also detected in the  $P(1)$  line. The position of the  $^{13}\text{CN}$   $R(0)$  line corresponding to the stronger of the two components is indicated by a tick mark. Since the  $R(2)$  and  $P(2)$  lines are below the detection limit, no fits were attempted for these features.

$^{13}\text{CH}^+$  absorption is detected toward HD 152236 nor toward HD 210121 due to the low column densities of the individual  $^{12}\text{CH}^+$  components in these directions. For HD 154368, HD 161056, and HD 169454, the  $^{12}\text{CH}^+$  absorption profiles at 4232 Å are almost certainly blended with  $^{13}\text{CH}^+$ , making it difficult to obtain any meaningful results on the  $^{12}\text{CH}^+ / ^{13}\text{CH}^+$  ratio. For sight lines with simpler profiles, the results are more encouraging, but the uncertainties are still quite large. The  $^{12}\text{CH}^+$  and  $^{13}\text{CH}^+$  features in the spectrum of HD 170740 do not appear to be blended, but  $^{13}\text{CH}^+$  is only detected at the 1.4- $\sigma$  level. The sight line to HD 73882 permits a relatively clean detection of both  $^{12}\text{CH}^+$  and  $^{13}\text{CH}^+$  at 4232 Å, though the continuum level is somewhat uncertain. Nevertheless, we find a  $^{12}\text{CH}^+ / ^{13}\text{CH}^+$  ratio in this direction of  $61.7 \pm 17.3$  for a fixed isotope shift of  $\Delta v = -18.9 \text{ km s}^{-1}$ .

We also analyzed the available UVES data on  $\text{CH}^+$  toward 23 Tau and  $\zeta$  Oph, both of which have simple, well-studied  $\text{CH}^+$  absorption profiles. From the (0, 0) transition at 4232 Å, we obtained a  $^{12}\text{CH}^+ / ^{13}\text{CH}^+$  ratio of  $102.3 \pm 38.4$  for 23 Tau ( $\Delta v = -19.4 \text{ km s}^{-1}$ ) and  $88.5 \pm 11.4$  for  $\zeta$  Oph ( $\Delta v = -19.0 \text{ km s}^{-1}$ ). However, independent fits to the (1, 0) line at 3957 Å yielded lower values ( $55.5 \pm 29.4$  for 23 Tau and  $52.8 \pm 9.1$  for  $\zeta$  Oph).

Taking the weighted mean of the two results in each case gives  $72.8 \pm 23.3$  for 23 Tau and  $66.7 \pm 7.1$  for  $\zeta$  Oph, both of which are consistent with the  $^{12}\text{CH}^+ / ^{13}\text{CH}^+$  ratios we derive from our McDonald observations of these stars (see Table 7). Still, the disparity in the values obtained from the two transitions highlights the problems encountered when attempting to fit the undulating continuum in the UVES spectra examined here. Given the uncertainties, our UVES results are not altogether dissimilar to those of Casassus et al. (2005) and Stahl et al. (2008), who first analyzed these data. Casassus et al. found a  $^{12}\text{CH}^+ / ^{13}\text{CH}^+$  ratio of  $78.5 \pm 3.5$  for the sight line to  $\zeta$  Oph, while Stahl et al., reanalyzing the  $\zeta$  Oph data, obtained a ratio of  $80.9 \pm 3.0$ . In the direction of 23 Tau, Stahl et al. found  $^{12}\text{CH}^+ / ^{13}\text{CH}^+ = 96.5 \pm 16.3$ , while toward HD 73882, these authors obtained a  $^{12}\text{CH}^+ / ^{13}\text{CH}^+$  ratio of  $79.7 \pm 14.5$ .

The weaker lines of the  $B-X$  (0, 0) band in CN were fitted using the component structure found for the  $R(0)$  line. Since the majority of CN absorption profiles consist of single velocity components, this restriction essentially amounted to keeping the  $b$ -values fixed. In cases where an additional component is observed, the velocity difference between the two components, as determined from the  $R(0)$  line, was also held constant. The strengths of the

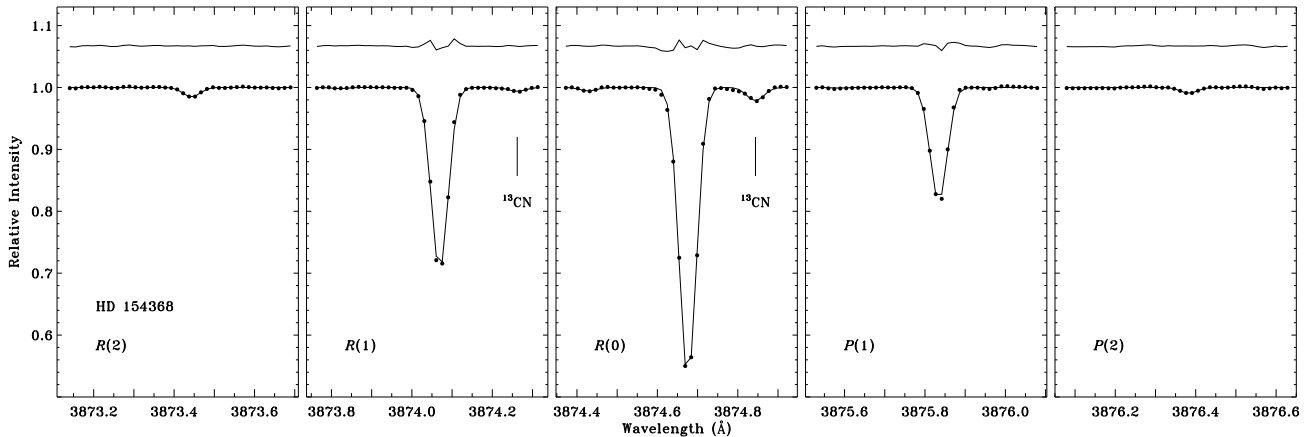


**Figure 14.** Same as Figure 12 except for the CN  $B-X$  (0, 0) band toward HD 154368. The positions of the  $R(0)$  and  $R(1)$  lines of  $^{13}\text{CN}$  are indicated by tick marks. The weak absorption feature blueward of the strong  $^{12}\text{CN}$   $R(0)$  line is due to a second very weak component along the line of sight, which is positively identified in the spectra of  $\text{CH}^+$  and  $\text{CH}$ .

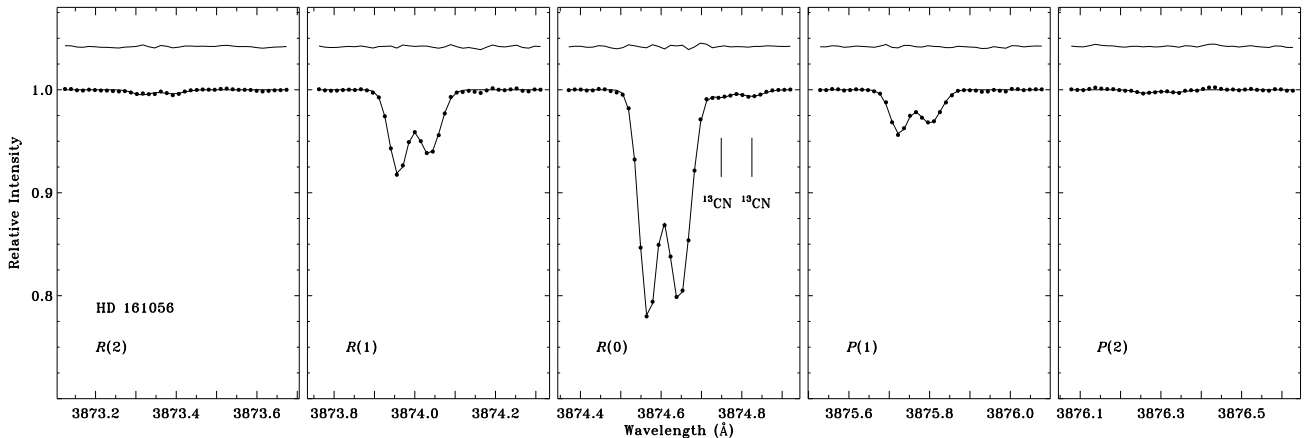


**Figure 15.** Same as Figure 12 except for the CN  $B-X$  (0, 0) band toward HD 161056. Two components of approximately equal strength are identified in each of the  $^{12}\text{CN}$  lines. The positions of the  $^{13}\text{CN}$   $R(0)$  lines corresponding to these components are indicated by tick marks.

individual components were allowed to vary, however, so that excitation temperatures could be derived separately for each cloud along the line of sight. Although two lines arising from the same excitation state, such as  $R(1)$  and  $P(1)$  or  $R(2)$  and  $P(2)$ , should yield identical column densities, each line was synthesized independently in our analysis. The final column density for a given  $N = 1$  or  $N = 2$  level was then determined by taking the weighted mean of the two results. Table 9 presents the CN column densities for each rotational level with a detectable transition. For the four UVES sight lines where  $^{13}\text{CN}$   $R(1)$  is detected, the  $R(1)$  lines of both isotopologues were fitted simultaneously as in the case of  $R(0)$ . The same technique was applied to the  $P(1)$  lines of  $^{12}\text{CN}$  and  $^{13}\text{CN}$  in the direction of HD 169454. Because this procedure permits the 12-to-13 ratios in different  $N$  levels to vary, we can accommodate small variations in excitation temperature between  $^{12}\text{CN}$  and  $^{13}\text{CN}$ . Figures 12 through 18 give the profile synthesis fits to the CN  $B-X$  (0, 0) band for each of the UVES sight lines.

Since the isotope shifts in CN and  $\text{CH}^+$  were left as free parameters during profile synthesis, it is instructive to compare our results, from astronomical spectra, with those obtained in laboratory experiments. The mean isotope shift in our synthesis fits of the  $\text{CH}^+$

(0, 0) transition at 4232 Å (toward McDonald targets) is  $\Delta v = -18.9 \pm 0.4 \text{ km s}^{-1}$  ( $\delta\lambda = -0.267 \pm 0.005 \text{ \AA}$ ). This result is consistent with the experimental value of  $-19.3 \pm 0.3 \text{ km s}^{-1}$  ( $-0.272 \pm 0.004 \text{ \AA}$ ), which is based on the laboratory measurements of Carrington & Ramsay (1982) for  $^{12}\text{CH}^+$  and Bembenek (1997) for  $^{13}\text{CH}^+$ . Similarly, our mean isotope shift for the CN (0, 0)  $R(0)$  line,  $\Delta v = +13.1 \pm 0.4 \text{ km s}^{-1}$  ( $\delta\lambda = +0.169 \pm 0.005 \text{ \AA}$ ), agrees favorably with the laboratory value,  $\Delta v = +13.6 \text{ km s}^{-1}$  ( $\delta\lambda = +0.176 \text{ \AA}$ ; Bakker & Lambert 1998). The four detections of  $^{13}\text{CN}$   $R(1)$  yield a mean isotope shift for the  $R(1)$  line of  $+14.6 \pm 0.4 \text{ km s}^{-1}$  ( $+0.188 \pm 0.005 \text{ \AA}$ ), while, from the  $^{12}\text{CN}$  and  $^{13}\text{CN}$   $P(1)$  lines observed toward HD 169454, we derive an isotope shift of  $+9.2 \pm 0.4 \text{ km s}^{-1}$  ( $+0.118 \pm 0.005 \text{ \AA}$ ). The laboratory results give  $+14.8 \text{ km s}^{-1}$  ( $+0.192 \text{ \AA}$ ) for the  $R(1)$  line blend and  $+10.0 \text{ km s}^{-1}$  ( $+0.130 \text{ \AA}$ ) for the  $P(1)$  blend (Bakker & Lambert 1998). The generally good agreement between the laboratory and astronomical results serves as confirmation that our detections of the  $^{13}\text{CN}$   $R(1)$  and  $P(1)$  lines are real.

#### 4. ISOTOPOLOGIC RATIOS IN C-BEARING MOLECULES

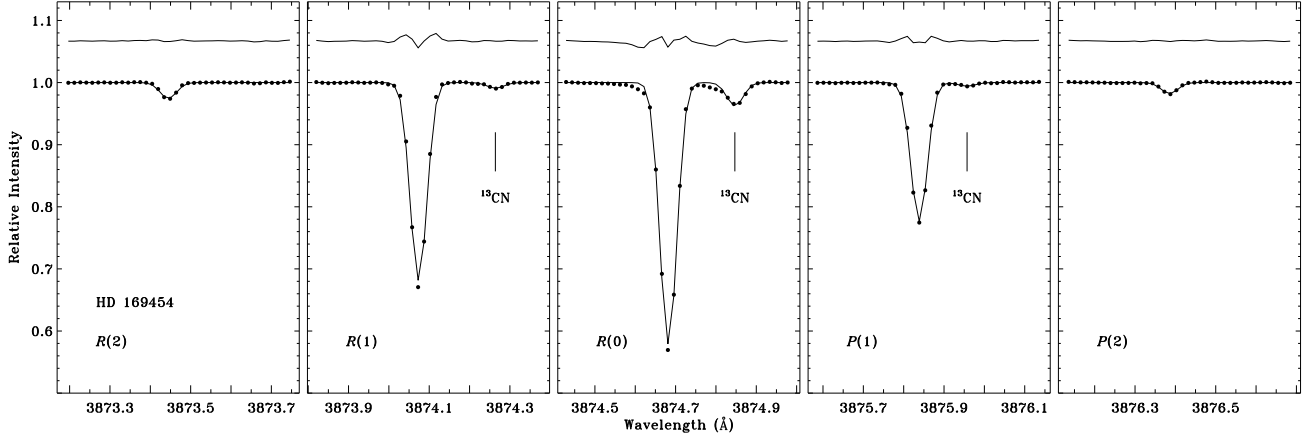


**Figure 16.** Same as Figure 12 except for the CN  $B-X$  (0, 0) band toward HD 169454. The positions of the  $R(0)$ ,  $R(1)$ , and  $P(1)$  lines of  $^{13}\text{CN}$  are indicated by tick marks.

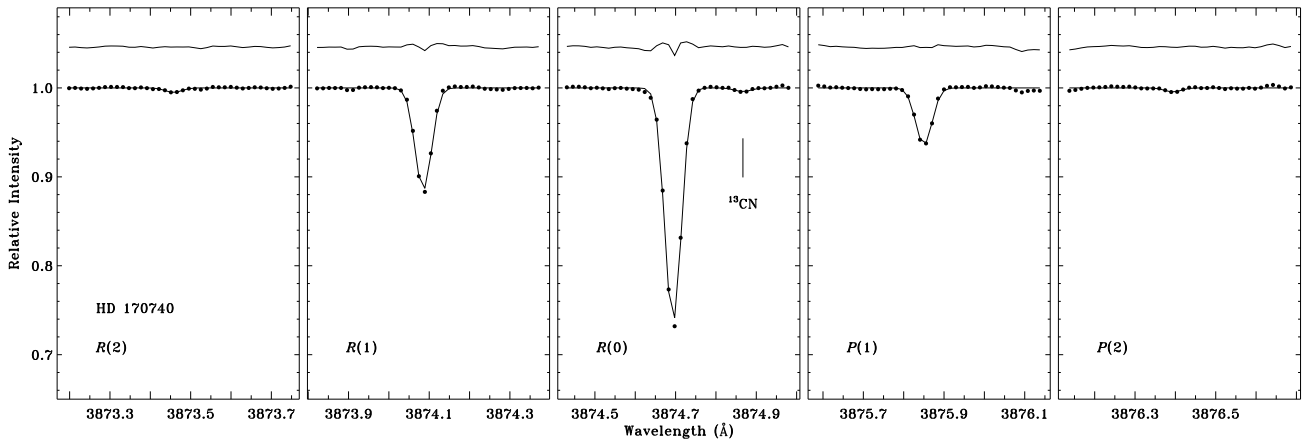


**Figure 17.** Same as Figure 12 except for the CN  $B-X$  (0, 0) band toward HD 170740. The position of the  $^{13}\text{CN}$   $R(0)$  line is indicated by a tick mark.

#### 4.1. $^{12}\text{CH}^+ / ^{13}\text{CH}^+$ Ratios

One of the primary motivations for this study was to evaluate whether the reported variations in the  $^{12}\text{CH}^+ / ^{13}\text{CH}^+$  ratio toward stars in the solar neighborhood are indicative of intrinsic scatter in the local interstellar  $^{12}\text{C} / ^{13}\text{C}$  ratio or result instead from systematic effects in the individual investigations. The results of our detailed analysis suggest that the latter scenario is more likely. In particular, we do not confirm the low ratios that were obtained by Hawkins & Jura (1987) from Lick Observatory data toward the Pleiades stars 20 Tau and 23 Tau ( $40 \pm 9$  and  $41 \pm 9$ , respectively), nor an earlier result toward 20 Tau ( $49_{-8}^{+12}$ ) by Vanden Bout & Snell (1980). Hawkins et al. (1985, 1989) reported low  $^{12}\text{CH}^+ / ^{13}\text{CH}^+$  ratios based on Lick data toward  $\zeta$  Oph, as well, giving values of  $43 \pm 6$  (Hawkins et al. 1985) and  $49 \pm 10$  (Hawkins et al. 1989). However, many subsequent investigations revealed  $^{12}\text{CH}^+ / ^{13}\text{CH}^+$  ratios closer to 70 for this line of sight, including Hawkins et al. (1993), who examined Kitt Peak National Observatory (KPNO) spectra of  $\zeta$  Oph, arriving at a ratio of  $63 \pm 8$ . More precise results are available from Crane et al. (1991), who used the 2.7 m telescope at McDonald Observatory to derive a  $^{12}\text{CH}^+ / ^{13}\text{CH}^+$  ratio of  $67.6 \pm 4.5$ , and Stahl & Wilson (1992), who reanalyzed ESO observations of  $\zeta$  Oph (Stahl et al. 1989) and found a value of  $71 \pm 3$ .

The Crane et al. (1991) result is, in fact, very close to the mean value of all of the  $\zeta$  Oph results reported in the literature. Our new determination from McDonald data, while not as precise as the Crane et al. (1991) value, is nonetheless consistent with it.

Hawkins et al. (1993) believe that the discrepancies between their KPNO results and the earlier Lick results for  $\zeta$  Oph (e.g., Hawkins et al. 1985) were caused by telluric contamination of the Lick spectra, which complicated the placement of the continuum. While this explanation may have resolved the controversy surrounding the  $^{12}\text{CH}^+ / ^{13}\text{CH}^+$  ratio toward  $\zeta$  Oph, it left open the possibility that the spectra obtained by Hawkins & Jura (1987), including for 20 Tau and 23 Tau, were not similarly contaminated and that the low  $^{12}\text{CH}^+ / ^{13}\text{CH}^+$  ratios in these directions would later be confirmed. With our new results on  $^{12}\text{CH}^+ / ^{13}\text{CH}^+$  toward 20 Tau and 23 Tau, such a position would now be difficult to support. The Stahl et al. (2008) value for  $^{12}\text{CH}^+ / ^{13}\text{CH}^+$  in the direction of 23 Tau ( $96.5 \pm 16.3$ ) is further confirmation that a ratio closer to 40 in the Pleiades clouds is unlikely, although the UVES results have their own complications (see § 3). Initially, we suspected that the difference between our McDonald results and those of Hawkins & Jura (1987) for the Pleiades stars was related to the smaller  $b$ -values we derive when modeling

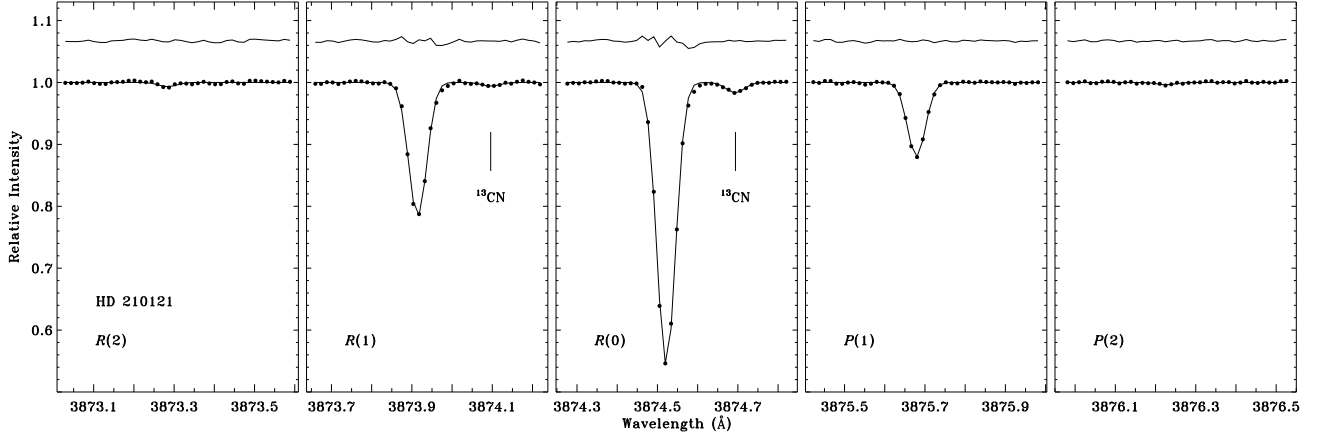


**Figure 18.** Same as Figure 12 except for the CN  $B-X$  (0, 0) band toward HD 210121. The positions of the  $R(0)$  and  $R(1)$  lines of  $^{13}\text{CN}$  are indicated by tick marks.

the CH<sup>+</sup> profiles. However, our optical depth corrections for these sight lines, as determined by the profile fitting routine, would only amount to increases of about 4% in  $N(^{12}\text{CH}^+)$  over the column densities obtained by Hawkins & Jura (1987) from their adopted corrections, whereas the  $^{12}\text{CH}^+/^{13}\text{CH}^+$  ratios differ by a factor of 2. The dominant cause of the discrepancy is the almost factor-of-2 larger equivalent widths that Hawkins & Jura (1987) find for the  $^{13}\text{CH}^+$  lines (see Table 2), which again points to possible errors in continuum normalization or to the effects of blending in their more moderate resolution spectra.

Federman et al. (2003) analyzed McDonald 2.7 m data toward  $\rho$  Oph A and found a  $^{12}\text{CH}^+/^{13}\text{CH}^+$  ratio of  $120 \pm 54$ , which, despite the large value, is within  $1 \sigma$  of our more precise determination. These authors achieved a S/N ratio per pixel of about 650 in the vicinity of CH<sup>+</sup>  $\lambda 4232$ , whereas the S/N is about 950 per pixel in our  $\rho$  Oph A data. As our spectra were also sampled at slightly higher resolution, this case illustrates the general trend that higher-resolution, higher signal-to-noise observations tend to result in  $^{12}\text{CH}^+/^{13}\text{CH}^+$  ratios that are closer to the average interstellar value of  $^{12}\text{C}/^{13}\text{C}$ . Indeed, our McDonald observations of 20 Tau, 23 Tau,  $\rho$  Oph A, and  $\zeta$  Oph yield  $^{12}\text{CH}^+/^{13}\text{CH}^+$  ratios that are indistinguishable from 70 in each case. The weighted mean of the four determinations is  $74.4 \pm 7.6$ , or only  $0.6 \sigma$  higher than the  $^{12}\text{C}/^{13}\text{C}$  ratio adopted for the local interstellar medium. While this mean represents only a small sample of interstellar sight lines, the result is significant in the sense that each of these sight lines at one time had been found to have a much lower or much higher  $^{12}\text{CH}^+/^{13}\text{CH}^+$  ratio. The statistical dispersion (i.e., standard deviation) in our new determinations of  $^{12}\text{CH}^+/^{13}\text{CH}^+$  for these four sight lines (7.3) is essentially identical to the error in the weighted mean (7.6). We interpret these findings as confirmation of the theoretical expectation that  $^{12}\text{CH}^+/^{13}\text{CH}^+$  reflects the ambient carbon isotopic ratio, and that this ratio does not vary within the solar neighborhood.

#### 4.2. $^{12}\text{CN}/^{13}\text{CN}$ Ratios

The  $^{12}\text{CN}/^{13}\text{CN}$  ratios presented in Table 7 constitute the most extensive isotopologic results to date for CN in diffuse molecular clouds. The UVES results, in partic-

ular, are considerably more precise than any literature results currently available. Gredel et al. (1991) reported abundance ratios of  $^{12}\text{CN}$  to  $^{13}\text{CN}$  for four interstellar sight lines. These included HD 73882 and HD 169454, for which they found  $^{12}\text{CN}/^{13}\text{CN}$  ratios of  $170 \pm 120$  and  $38 \pm 16$ , respectively. Due to the large uncertainties, these authors were unable to conclude whether or not the scatter in their sample represented true cloud-to-cloud variations. Our new results for these lines of sight reveal  $^{12}\text{CN}/^{13}\text{CN}$  ratios closer to the ambient value of  $^{12}\text{C}/^{13}\text{C}$  in both instances. However, the small uncertainties in our determinations allow even modest variations in the relative abundances of  $^{12}\text{CN}$  and  $^{13}\text{CN}$  to be discerned. Thus, the moderate increase in  $^{12}\text{CN}/^{13}\text{CN}$  that we find toward HD 73882 likely indicates an actual deficit in  $^{13}\text{CN}$ , relative to  $^{12}\text{CN}$ , for the gas in this direction. Further confirmation of our result comes from an independent assessment by D. Welty (private communication), who finds a  $^{12}\text{CN}/^{13}\text{CN}$  ratio of 87 for the line of sight to HD 73882. For HD 154368, Palazzi et al. (1990) reported a  $^{12}\text{CN}/^{13}\text{CN}$  ratio of  $101 \pm 12$ , whereas we find a value essentially equal to 70. In this case, and in the comparison with the Gredel et al. (1991) results, the discrepancy in the  $^{12}\text{CN}/^{13}\text{CN}$  ratio is largely driven by differences in the measured equivalent width of the  $^{13}\text{CN}$  line (see Table 3). However, the Gredel et al. (1991) values of  $W_\lambda(^{13}\text{CN})$  only differ from ours at the  $1-\sigma$  level, because of their significantly larger uncertainties, whereas the Palazzi et al. (1990) measurement of  $W_\lambda(^{13}\text{CN})$  for HD 154368 ( $0.82 \pm 0.10$  mÅ) is lower than our more precise result ( $1.13 \pm 0.04$  mÅ) by  $3 \sigma$ . Equivalent width measurements of very weak lines are particularly sensitive to the placement of the continuum. However, by examining the raw (unnormalized) spectrum of HD 154368, we can find no acceptable continuum fit that would yield a value of  $W_\lambda(^{13}\text{CN})$  as low as the Palazzi et al. (1990) result.

Of the McDonald sight lines, both  $\zeta$  Oph and  $\zeta$  Per have previously been investigated for  $^{12}\text{CN}/^{13}\text{CN}$ . The most precise result available is that of Crane & Hegyi (1988), who found a  $^{12}\text{CN}/^{13}\text{CN}$  ratio of  $47.3^{+5.5}_{-4.4}$  in the direction of  $\zeta$  Oph. Later, Roth & Meyer (1995) obtained a ratio of  $35 \pm 13$  for this line of sight. Our new determination ( $48.8 \pm 19.5$ ) has a precision comparable to the Roth & Meyer (1995) value, yet agrees well with the result of

Crane & Hegyi (1988). For  $\zeta$  Per, Kaiser et al. (1991) found a  $^{12}\text{CN}/^{13}\text{CN}$  ratio of  $77_{-18}^{+27}$ , which is consistent with the slightly less precise value we derive from our McDonald observations of this star ( $67.0 \pm 28.0$ ). In order to obtain a more precise result for  $\zeta$  Per, we can combine our determination with that of Kaiser et al. (1991) to arrive at a weighted mean  $^{12}\text{CN}/^{13}\text{CN}$  ratio of  $72 \pm 19$ . Thus, again, we find a value of  $^{12}\text{CN}/^{13}\text{CN}$  that is indistinguishable from the ambient  $^{12}\text{C}/^{13}\text{C}$  ratio. This is in contrast to the collection of  $\zeta$  Oph results, which provides strong evidence for a  $^{12}\text{CN}/^{13}\text{CN}$  ratio that is significantly lower than the ambient value. We have already noted the elevated  $^{12}\text{CN}/^{13}\text{CN}$  ratio we find in the direction of HD 73882, which is significant because of the small uncertainty. Meyer et al. (1989) find a  $^{12}\text{CN}/^{13}\text{CN}$  ratio of  $122 \pm 33$  toward HD 21483, which, despite the larger uncertainty, also suggests a higher-than-ambient value. Together, these results indicate that, unlike  $\text{CH}^+$ , CN is affected by fractionation in at least some diffuse environments.

The weighted mean of all of our determinations of  $^{12}\text{CN}/^{13}\text{CN}$  toward McDonald and UVES targets is  $67.5 \pm 1.0$ , which agrees well with the adopted value for the local interstellar  $^{12}\text{C}/^{13}\text{C}$  ratio. However, there is significant scatter in  $^{12}\text{CN}/^{13}\text{CN}$  from one sight line to another and the relatively small uncertainties in our determinations suggest that the variation represents true differences among the environments being probed. From our sample of  $^{12}\text{CN}/^{13}\text{CN}$  ratios, we find a dispersion of 24.9, which, in contrast to the situation for  $\text{CH}^+$ , is much greater than the error in the weighted mean (1.0). These results for CN are similar, statistically, to published results for CO. For example, the weighted mean value of  $^{12}\text{CO}/^{13}\text{CO}$  from the ratios tabulated by Sheffer et al. (2007) is  $69.9 \pm 1.9$ , while the dispersion in those measurements is 29.5. Again, this suggests a level of fractionation in CN (and CO) not observed in  $\text{CH}^+$ . However, some caution on this point may be warranted. First, we are unable to determine reliable  $^{12}\text{CH}^+ / ^{13}\text{CH}^+$  ratios for the majority of the UVES sight lines, meaning that our sample of  $\text{CH}^+$  ratios is considerably smaller than that for CN. Second, the CN ratios toward HD 161056 and HD 170740, the two sight lines contributing the most to the scatter in  $^{12}\text{CN}/^{13}\text{CN}$ , are somewhat uncertain. The  $^{12}\text{CN}$  and  $^{13}\text{CN}$  features are blended in the spectrum of HD 161056 because of the velocity separation between the two line-of-sight components. This may also contribute to the somewhat higher isotope shift we find in this direction. For HD 170740, there is some uncertainty in the placement of the continuum due to what may be either telluric absorption or the result of instrumental fringing just to the red of the  $^{13}\text{CN}$  feature, which is also quite weak. Without these two extreme results, the scatter in  $^{12}\text{CN}/^{13}\text{CN}$  is reduced to 10.3, though this might still be significant given the small error in the weighted mean value.

#### 4.3. $^{12}\text{CN}/^{13}\text{CN}$ versus $^{12}\text{CO}/^{13}\text{CO}$

Many of the targets selected for this investigation were chosen because they exhibit fractionated values of  $^{12}\text{CO}/^{13}\text{CO}$  (see Table 7). That is to say their  $^{12}\text{CO}/^{13}\text{CO}$  ratios are significantly above or below the ambient value of  $^{12}\text{C}/^{13}\text{C}$ . Since CN and CO are presumed to reside in the same portion of a diffuse molecular

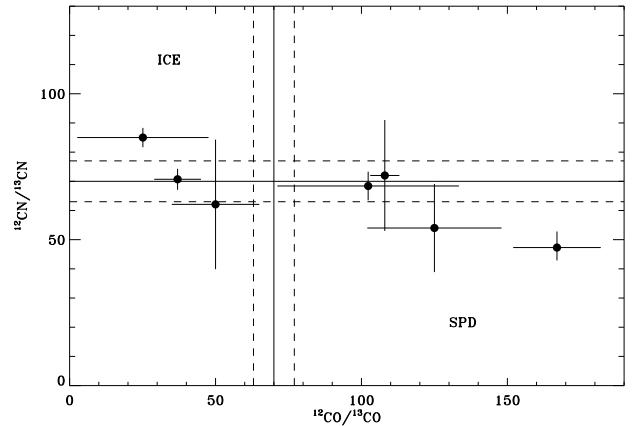


**Figure 19.**  $^{12}\text{CN}/^{13}\text{CN}$  versus  $^{12}\text{CO}/^{13}\text{CO}$  for the seven sight lines where both ratios have been determined. The solid and dashed lines denote the mean and  $1\text{-}\sigma$  deviations of the local interstellar  $^{12}\text{C}/^{13}\text{C}$  ratio ( $70 \pm 7$ ; see Sheffer et al. 2007). Data points in the upper left quadrant are influenced by isotopic charge exchange (ICE), while those in the lower right are dominated by selective photodissociation (SPD).

cloud (Pan et al. 2005), the expectation is that CN will be fractionated in the opposite sense compared to CO. This is due to the fact that CO is the most abundant C-bearing molecule in the ISM (by 2–3 orders of magnitude over CN), and should regulate the availability of  $^{13}\text{C}$  atoms for incorporation into other C-bearing molecules that are cospatial and must draw from the same carbon reservoir. Figure 19 plots  $^{12}\text{CN}/^{13}\text{CN}$  versus  $^{12}\text{CO}/^{13}\text{CO}$  for the seven sight lines where both ratios have been determined. The  $^{12}\text{CN}/^{13}\text{CN}$  ratios are from this investigation (Table 7) except in the case of  $\zeta$  Oph, where we have used the more precise determination by Crane & Hegyi (1988), and in the case of  $\zeta$  Per, where we have plotted the weighted mean of our result and that of Kaiser et al. (1991). The  $^{12}\text{CO}/^{13}\text{CO}$  ratios are either from our archival study using *HST* (Sheffer et al. 2007) or from the literature (Hanson et al. 1992; Sonnentrucker et al. 2007). Also indicated in the figure is the value we adopt for the local interstellar  $^{12}\text{C}/^{13}\text{C}$  ratio ( $70 \pm 7$ ; see Sheffer et al. 2007), which divides the parameter space into four quadrants. Two of these quadrants are of particular interest: the upper left quadrant, where low values of  $^{12}\text{CO}/^{13}\text{CO}$  are associated with high values of  $^{12}\text{CN}/^{13}\text{CN}$ , and the lower right quadrant, where high  $^{12}\text{CO}/^{13}\text{CO}$  and low  $^{12}\text{CN}/^{13}\text{CN}$  ratios coexist. In molecular gas characterized by a low  $^{12}\text{CO}/^{13}\text{CO}$  ratio, isotopic charge exchange has presumably converted some of the  $^{12}\text{CO}$  into  $^{13}\text{CO}$ , while also exchanging  $^{13}\text{C}^+$  ions for  $^{12}\text{C}^+$ . Since the formation of CN is initiated by reactions involving  $\text{C}^+$  (e.g., Federman et al. 1994), the gas in an environment where CO is fractionated by ICE should be enhanced in  $^{12}\text{CN}$  relative to  $^{13}\text{CN}$ . In contrast, a high  $^{12}\text{CO}/^{13}\text{CO}$  ratio indicates that the molecular gas has been subjected to selective photodissociation, which preferentially destroys  $^{13}\text{CO}$  when only  $^{12}\text{CO}$  is self shielded. In regions where SPD is occurring, the dissociated  $^{13}\text{C}$  atoms are quickly ionized and incorporated into the pathways that lead to CN, which should result in enhanced  $^{13}\text{CN}$  production.

The data plotted in Figure 19 are suggestive of the inverse relationship between  $^{12}\text{CN}/^{13}\text{CN}$  and  $^{12}\text{CO}/^{13}\text{CO}$

that is expected due to photochemical fractionation and the physical association of CN and CO in diffuse cloud cores. Virtually no data points populate the upper right or lower left quadrants of the figure where the fractionation of CN and CO occurs in the same directions. The two data points that do (just barely) lie in these regions are for the sight lines to 20 Aql (in the lower left) and  $\zeta$  Per (in the upper right). These sight lines have large uncertainties associated with their  $^{12}\text{CN}/^{13}\text{CN}$  ratios, which in both cases are consistent with the unfractionated value. Although the downward trend in  $^{12}\text{CN}/^{13}\text{CN}$  with increasing  $^{12}\text{CO}/^{13}\text{CO}$  is apparent, the correlation between these two parameters is rather shallow. In addition, the appearance of a trend is somewhat contingent upon the data points at the extremes. The sight line with the lowest  $^{12}\text{CO}/^{13}\text{CO}$  ratio (and highest value of  $^{12}\text{CN}/^{13}\text{CN}$ ) is HD 73882, while the highest values of  $^{12}\text{CO}/^{13}\text{CO}$  (and lowest  $^{12}\text{CN}/^{13}\text{CN}$  ratios) are found in the directions of  $\rho$  Oph A and  $\zeta$  Oph (in order of increasing  $^{12}\text{CO}/^{13}\text{CO}$ ). All of the  $^{12}\text{CN}/^{13}\text{CN}$  ratios between these extremes are consistent with the ambient value. Yet the uncertainties in  $^{12}\text{CN}/^{13}\text{CN}$  toward HD 73882 and  $\zeta$  Oph are among the smallest in the sample, giving credence to the perceived trend.

The severity of CN fractionation depends not only on the effects that alter the relative abundances of  $^{12}\text{CO}$  and  $^{13}\text{CO}$  but also on the balance between CO and C<sup>+</sup>, the other major reservoir of carbon in diffuse gas. If CO and C<sup>+</sup> have roughly equivalent abundances, then any alteration in  $^{12}\text{CO}/^{13}\text{CO}$  will have an equal, but opposite, effect on  $^{12}\text{C}^+ / ^{13}\text{C}^+$  and hence on  $^{12}\text{CN}/^{13}\text{CN}$ . If C<sup>+</sup> dominates over CO, however, fractionation in CO will have less of an impact on  $^{12}\text{CN}/^{13}\text{CN}$  because there will be a larger pool of C<sup>+</sup> ions that will maintain the ambient 12-to-13 ratio. The reverse is also true. When CO dominates, CO fractionation will have a greater influence on the ratio of  $^{12}\text{CN}$  to  $^{13}\text{CN}$ . A detailed modeling effort to track how the relative abundance of each isotope (and isotopologue) of interest depends on the physical conditions in the cloud and the parameters of the external UV radiation field is beyond the scope of this paper. Instead, we employ a simple, analytical method to estimate the fraction of carbon that is locked up in CO along a given line of sight based on the measured isotopologic ratios in CN and CO. In what follows, we define  $f(^{13}\text{CN}) = N(^{13}\text{CN})/[N(^{12}\text{CN}) + N(^{13}\text{CN})] = 1/[N(^{12}\text{CN})/N(^{13}\text{CN}) + 1]$  as the fraction of CN molecules that take the form of  $^{13}\text{CN}$ . Similar definitions can be made for  $^{13}\text{CO}$  and  $^{13}\text{CH}^+$ , where  $f(^{13}\text{CH}^+) \equiv f(^{13}\text{C}) = 1/(70 + 1) = 0.014$  is taken to be the ambient fraction of  $^{13}\text{C}$ . With these definitions, we can write  $f(^{13}\text{CN})$  as a function of  $f(^{13}\text{CO})$  and  $f(^{13}\text{CH}^+)$ . We have

$$\begin{aligned} f(^{13}\text{CN}) &= f(^{13}\text{CH}^+)[1 - x] \\ &\quad + \{f(^{13}\text{CH}^+) + [f(^{13}\text{CH}^+) - f(^{13}\text{CO})]\} x \\ &= f(^{13}\text{CH}^+) + [f(^{13}\text{CH}^+) - f(^{13}\text{CO})] x, \end{aligned} \quad (1)$$

where the factor  $x$  determines how strongly  $f(^{13}\text{CN})$  is affected by changes in  $f(^{13}\text{CO})$  and is equivalent to the column density ratio  $N(\text{CO})/N(\text{C}^+)$ , assuming the abundance of neutral carbon is negligible. In the limiting case  $x = 0$  [i.e.,  $N(\text{C}^+) \gg N(\text{CO})$ ], CN is unaffected by

fractionation in CO and  $^{12}\text{CN}/^{13}\text{CN}$  equals the ambient ratio.

Equation (1) can be rearranged to yield an expression for  $x$ ,

$$x = \frac{f(^{13}\text{CN}) - f(^{13}\text{CH}^+)}{f(^{13}\text{CH}^+) - f(^{13}\text{CO})}, \quad (2)$$

which is valid whether CO is fractionated upward via selective photodissociation or downward due to isotopic charge exchange. However, when selective photodissociation is under consideration, the fractions should be defined as, for example,  $f(^{13}\text{CN}) = N(^{13}\text{CN})/N(^{12}\text{CN})$ , because SPD does not exchange one isotopologue for another but simply destroys the less abundant isotopologue leaving the more abundant one unchanged. The fraction of total carbon that is locked up in CO can be found from  $x$  by  $f(\text{CO}) = N(\text{CO})/[N(\text{CO}) + N(\text{C}^+)] = [N(\text{CO})/N(\text{C}^+)]/[N(\text{CO})/N(\text{C}^+) + 1] = x/(x + 1)$ . We use this relation in conjunction with equation (2) to derive  $f(\text{CO})$  for the sight lines included in Figure 19. The resulting values are  $f(\text{CO}) = 0.09$  for HD 73882, 0.01 for HD 154368, 0.07 for HD 210121, 0.40 for  $\rho$  Oph A, and 0.45 for  $\zeta$  Oph. No physically meaningful determinations of  $f(\text{CO})$  are possible toward 20 Aql or  $\zeta$  Per because the measured isotopologic ratios in CN and CO fall on the same side of the ambient ratio. Again, we note that in these cases the  $^{12}\text{CN}/^{13}\text{CN}$  ratios are consistent with being unfractionated.

For the sight lines in Ophiuchus, we find that nearly 50% of the carbon is contained in CO, which is consistent with the fact that the UV optical depths ( $\tau_{\text{UV}} = 1.98$  and 2.04 for the clouds toward  $\zeta$  Oph and  $\rho$  Oph A, respectively) are near that where the C<sup>+</sup> to CO conversion is expected to occur (i.e.,  $\tau_{\text{UV}} = 2$ ; see Federman et al. 1994). The value of  $f(\text{CO})$  is substantially lower toward HD 210121 even though the UV optical depth in this direction ( $\tau_{\text{UV}} = 3.35$ ; Sheffer et al. 2008) is larger than those for the Ophiuchus clouds. Here, we note that the  $^{12}\text{CO}/^{13}\text{CO}$  ratio in the direction of HD 210121 is consistent with 70 and so does not show strong evidence of fractionation, meaning that  $f(\text{CO})$  cannot be determined. An unfractionated value of  $^{12}\text{CO}/^{13}\text{CO}$  toward HD 210121 is also consistent with the suggestion by Welty & Fowler (1992) that the UV radiation field incident on the cloud in this direction (the high-latitude molecular cloud DBB 80; see de Vries & van Dishoeck 1988) is lower than the average interstellar field. Finally, the low values of  $f(\text{CO})$  we find toward HD 73882 and HD 154368 are surprising considering the much larger UV optical depths in these directions (adopting  $\tau_{\text{UV}} \simeq 2A_V \simeq 4.7$  in both cases). The larger values of  $\tau_{\text{UV}}$  indicate that the sight lines to HD 73882 and HD 154368 probe deeper into their respective clouds, where a majority of the carbon is expected to be in the form of CO rather than in neutral atomic or ionic form. However, equation (2) only applies if the  $^{12}\text{CN}/^{13}\text{CN}$  ratio reflects the  $^{12}\text{C}^+ / ^{13}\text{C}^+$  ratio of the gas from which CN formed. If  $^{12}\text{CN}/^{13}\text{CN}$  is substantially altered after CN formation, then equation (2) no longer holds. Thus, instead of surmising that there is a very low fraction of elemental carbon in CO in the lines of sight to HD 73882 and HD 154368, we suggest that we are seeing the effects of a separate fractionation process in CN, which acts to

lower  $^{12}\text{CN}/^{13}\text{CN}$  such that the enhancements due to CO fractionation are not as large as expected.

We assume that the low  $^{12}\text{CO}/^{13}\text{CO}$  ratios in the directions of HD 73882 and HD 154368 result from an efficient isotopic charge exchange reaction involving CO, which implies a colder kinetic temperature for the molecular gas along these lines of sight. Yet, at colder temperatures, CN is similarly affected by ICE via the reaction  $^{13}\text{C}^+ + ^{12}\text{CN} \rightarrow ^{12}\text{C}^+ + ^{13}\text{CN} + \Delta E$ , where the zero-point energy difference  $\Delta E/k_B = 31$  K (Bakker & Lambert 1998; derived from the molecular parameters in Prasad et al. 1992) favors  $^{13}\text{CN}$ . Unlike CO, however, CN is dissociated by continuum radiation, not by lines, and so isotope-selective self shielding should not be a factor. Any dissociating photons will equally destroy  $^{12}\text{CN}$  as well as  $^{13}\text{CN}$ . Yet if the timescale for the ICE reaction with CN is shorter than the photodissociation timescale, then the reaction will reach equilibrium and we can write

$$\frac{n(^{12}\text{CN})}{n(^{13}\text{CN})} = \frac{n(^{12}\text{C}^+) k_r}{n(^{13}\text{C}^+) k_f} = \frac{n(^{12}\text{C}^+)}{n(^{13}\text{C}^+)} \exp\left(-\frac{\Delta E}{k_B T_{\text{kin}}}\right), \quad (3)$$

where  $n(X)$  represents the number density of species X,  $k_f$  is the rate coefficient of the forward reaction, and  $k_r = k_f \exp(-\Delta E/k_B T_{\text{kin}})$  is the rate coefficient of the reverse reaction. Analogous expressions have been derived in the case of CO (see Sheffer et al. 1992; Lambert et al. 1994). When photodissociation of CN dominates over isotopic charge exchange, no upward fractionation occurs, as it does for CO, because the photodissociation rates of the two CN isotopologues are equal (i.e.,  $\Gamma_{12} = \Gamma_{13}$ ) and we have

$$\frac{n(^{12}\text{CN})}{n(^{13}\text{CN})} = \frac{n(^{12}\text{C}^+) \Gamma_{13}}{n(^{13}\text{C}^+) \Gamma_{12}} = \frac{n(^{12}\text{C}^+)}{n(^{13}\text{C}^+)}. \quad (4)$$

It is important to note that the  $^{12}\text{C}^+/^{13}\text{C}^+$  ratio in equations (3) and (4) refers to the ratio that has been elevated above the ambient value of  $^{12}\text{C}/^{13}\text{C}$  by isotopic charge exchange with CO. Thus, when isotopic charge exchange with CN lowers  $^{12}\text{CN}/^{13}\text{CN}$ , this ratio is still higher than the ambient value. If we adopt a kinetic temperature of 51 K for the clouds toward HD 73882 and HD 154368, a value which corresponds to the observed  $\text{H}_2$  rotational temperature ( $T_{01}$ ) for both sight lines (Rachford et al. 2002), then we find, from equation (3), that ICE would have lowered  $^{12}\text{CN}/^{13}\text{CN}$  by a factor of 1.84. If the actual  $^{12}\text{C}^+/^{13}\text{C}^+$  ratios toward HD 73882 and HD 154368 are higher than the measured  $^{12}\text{CN}/^{13}\text{CN}$  ratios by this amount, then the values of  $f(\text{CO})$  in these directions would be 0.24 and 0.34, respectively. However, the rotational excitation temperature in  $\text{C}_2$  ( $T_{02}$ ) may provide a better indication of the kinetic temperature in the denser central portion of a diffuse cloud where CN resides. Indeed, Sonnentrucker et al. (2007) find that  $T_{02}(\text{C}_2)$  is consistently lower than  $T_{01}(\text{H}_2)$  for a given sight line. These authors fit theoretical models for the excitation to the observed  $\text{C}_2$  rotational level populations to estimate the actual kinetic temperature, finding  $T_{\text{kin}} = 20 \pm 5$  K for both HD 73882 and HD 154368. At this kinetic temperature, the true  $^{12}\text{C}^+/^{13}\text{C}^+$  ratios would be a factor of 4.71 higher than  $^{12}\text{CN}/^{13}\text{CN}$ , resulting in  $f(\text{CO})$  values of 0.32 for HD 73882 and 0.48 for HD 154368. Thus,

the inclusion of an isotopic charge exchange reaction with CN leads to more realistic values for the fraction of C in CO for sight lines with low  $^{12}\text{CO}/^{13}\text{CO}$  ratios. However, even at 20 K, the derived value of  $f(\text{CO})$  toward HD 73882 is smaller than would be expected. With our simple analytical model, it is difficult to accommodate a  $^{12}\text{CO}/^{13}\text{CO}$  ratio as low as 25 and also demand that a high fraction of carbon be locked up in CO. The uncertainty in the determination of  $^{12}\text{CO}/^{13}\text{CO}$  toward HD 73882 is considerable, however, and indicates that a ratio as high as 47 would be consistent with the observations. At  $T_{\text{kin}} = 20$  K, a  $^{12}\text{CO}/^{13}\text{CO}$  ratio of 47 would result in a value of  $f(\text{CO}) = 0.63$  for HD 73882. In the case of HD 154368, the maximum  $^{12}\text{CO}/^{13}\text{CO}$  ratio allowed by the much smaller reported uncertainty is 45, which, at  $T_{\text{kin}} = 20$  K, would yield  $f(\text{CO}) = 0.59$ . As these calculations demonstrate, there is a real need for expanding on existing chemical models of diffuse clouds in order to clarify the situation regarding photochemical fractionation in all of the relevant C-bearing molecules and atomic carbon species.

## 5. CN ROTATIONAL EXCITATION

The CN column densities resulting from our profile synthesis fits to the  $B-X(0,0)$  band can be used to derive the CN rotational excitation temperatures  $T_{01}$  and  $T_{12}$  by applying the Boltzmann equation

$$T_{ij} = \frac{h\nu}{k_B} \left[ \ln \left( \frac{g_j N_i}{g_i N_j} \right) \right]^{-1}, \quad (5)$$

where  $g$  and  $N$  denote the statistical weight and column density of the lower ( $i$ th) or upper ( $j$ th) rotational level. The energy separation associated with the  $N = 1-0$  transition at  $\lambda = 2.64$  mm is taken to be  $h\nu/k_B = 5.445$  K, while for  $N = 2-1$  at  $\lambda = 1.32$  mm, we assume  $h\nu/k_B = 10.885$  K (Black & van Dishoeck 1991). Uncertainties in  $T_{ij}$  were calculated from the column density uncertainties ( $\sigma_N$ ) through standard error propagation such that

$$\sigma_{T_{ij}} = \frac{h\nu}{k_B} \left[ \ln \left( \frac{g_j N_i}{g_i N_j} \right) \right]^{-2} \left[ \left( \frac{\sigma_{N_i}}{N_i} \right)^2 + \left( \frac{\sigma_{N_j}}{N_j} \right)^2 \right]^{1/2}. \quad (6)$$

The excitation temperatures and  $1-\sigma$  errors obtained from equations (5) and (6) are listed in Table 9, along with the column densities of  $^{12}\text{CN}$  in the first three rotational levels of the ground vibrational state. Also shown are the values of  $T_{01}$  for the  $^{13}\text{CN}$  molecule for the four UVES sight lines with detections of  $^{13}\text{CN} R(1)$ . For HD 73882, HD 154368, and HD 210121, the  $N = 1$  column density of  $^{13}\text{CN}$  is based solely on the value obtained from the  $R(1)$  line. Since both the  $R(1)$  and  $P(1)$  lines of  $^{13}\text{CN}$  are detected in the spectrum of HD 169454, the final value of  $N(N = 1)$  for  $^{13}\text{CN}$  in this direction is the weighted mean of the column densities derived from the two transitions.

As expected, our derived rotational temperatures are consistent with the dominant excitation mechanism being radiative pumping from the cosmic microwave background (see Figure 20). The weighted mean value of  $T_{01}(^{12}\text{CN})$  in our sample is  $2.754 \pm 0.002$  K, which implies



an excess over the temperature of the CMB ( $T_{\text{CMB}} = 2.725 \pm 0.002$  K; Mather et al. 1999) of only  $29 \pm 3$  mK. This modest excess likely arises from local collisional excitation by electrons in some environments (see below). However, the dispersion in individual values of  $T_{01}$  (134 mK) cautions that the excess may not be physical but rather due to measurement or modeling uncertainties in our analysis. There is a slight indication of a greater excess in  $T_{12}$  ( $^{12}\text{CN}$ ) based on the weighted mean of  $2.847 \pm 0.014$  K, but the dispersion in these measurements (262 mK) is also greater. An elevated value of  $T_{12}$  could be caused by an overestimation of the strength of the weak  $R(2)$  and  $P(2)$  lines, resulting from noise in the spectrum. This is likely to blame for the higher values of  $T_{12}$  we find toward the McDonald targets, as well as toward HD 161056 and HD 170740. These are the sight lines with the weakest CN absorption in our sample. For the directions where CN absorption is the strongest, namely, HD 73882, HD 154368, HD 169454, and HD 210121, the agreement between  $T_{01}$  and  $T_{12}$  is at the 3% level or better. The rotational excitation temperatures derived from the observed  $^{13}\text{CN}$   $R(0)$ ,  $R(1)$ , and  $P(1)$  lines show no excess over the temperature of the CMB. Quantitatively, the weighted mean value of  $T_{01}$  ( $^{13}\text{CN}$ ) is  $2.652 \pm 0.069$  K, which is within  $1 \sigma$  of  $T_{\text{CMB}}$ .

Recently, a compilation of CN excitation temperatures along over 100 lines of sight was published by Slyk et al. (2008). These authors claim to detect an excess over the cosmic microwave background of 580 mK based on their average temperature of 3.31 K. Upon closer inspection, however, the rather high values of  $T_{01}$  given in Slyk et al. (2008) are almost certainly the result of not accounting adequately for optical depth effects in the strong  $R(0)$  line. While the authors make numerous attempts at estimating the Doppler widths, they settle on a simple assumption that  $b = 1.0$  km s<sup>-1</sup> for all directions. In our much smaller sample, the vast majority of CN components have  $b < 1.0$  km s<sup>-1</sup> and we note that differences of only a few tenths of a km s<sup>-1</sup> can greatly impact the derived column densities, even for lines with moderate optical depths. If we restrict the Slyk et al. (2008) sample to only the eleven sight lines in common with our investigation, then their average excitation temperature is still 3.30 K. The largest discrepancies between the two samples arise for the three sight lines with the most severe cases of optically thick absorption, HD 73882, HD 154368, and HD 169454, for which Slyk et al. (2008) give  $T_{01} = 3.68$  K, 3.67 K, and 5.06 K, respectively. In each of these cases, their measured values of  $W_\lambda$  agree with ours at the 5% level. However, their column densities, especially those derived from the  $R(0)$  line, are significantly smaller than ours [by 40% for the  $R(0)$  lines toward HD 73882 and HD 154368 and 76% in the case of  $R(0)$  toward HD 169454]. The smaller values Slyk et al. infer for  $N(N=0)$  are then directly responsible for their higher values of  $T_{01}$ .

Palazzi et al. (1992) previously examined CN rotational excitation in a sample of 34 interstellar sight lines, ten of which are included in our investigation. Their weighted mean of  $T_{01} = 2.817 \pm 0.022$  K is within  $3 \sigma$  of our more precise result. From their mean value, Palazzi et al. (1992) deduced an excess temperature of  $82 \pm 30$  mK, which would be 92 mK relative to the value

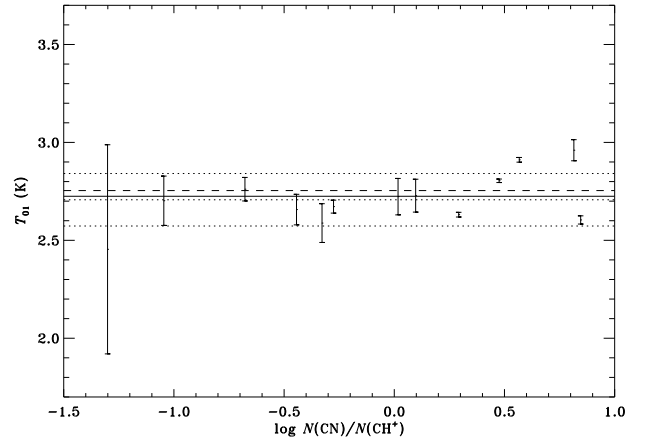


**Figure 20.** Rotational excitation temperatures in  $^{12}\text{CN}$  versus the  $\text{CN}/\text{CH}^+$  column density ratio for individual velocity components. The full  $3\text{-}\sigma$  range in  $T_{01}$  ( $^{12}\text{CN}$ ) is shown in each case. The solid line denotes the temperature of the Cosmic Microwave Background ( $T_{\text{CMB}} = 2.725$  K; Mather et al. 1999), while the dashed line represents the weighted mean value of  $T_{01}$  for our sample (2.754 K). The dotted lines indicate the (unweighted) mean and standard deviation for this set of measurements ( $2.707 \pm 0.134$  K). The two data points that lie above the  $1\text{-}\sigma$  range for the sample are for the main component toward HD 154368 and for the  $-3.1$  km s<sup>-1</sup> component toward HD 161056 (in order of increasing  $\text{CN}/\text{CH}^+$ ).

of  $T_{\text{CMB}}$  adopted here. Again, if we consider only the ten sight lines from Palazzi et al. (1992) that are also analyzed in the present work, their average excitation temperature is 2.813 K, which is essentially identical to their full sample mean. Evidently, sample size has little impact on the mean value of  $T_{01}$  ( $^{12}\text{CN}$ ), which is more heavily dependent on systematic effects, and, specifically, on corrections for optical depth. The basic difference between our study and that of Palazzi et al. (1992) is that, for the ten sight lines in common, Palazzi et al. find  $b$ -values that are, on average,  $0.1$  km s<sup>-1</sup> higher than the ones we derive. This is a minor difference, but it accounts for the 2% higher mean excitation temperature that these authors obtained. We also note that, for this sample of ten sight lines, we have reduced the scatter in  $T_{01}$  from  $0.3$  K to  $0.1$  K.

Although our mean CN excitation temperature ( $2.754 \pm 0.002$  K) implies a smaller excess over the temperature of the CMB ( $29 \pm 3$  mK) than has been found previously, our result has greater statistical significance because of the reduced uncertainties. However, two of the four sight lines in our sample with the strongest CN absorption lines, and therefore the smallest errors in  $T_{01}$ , have excitation temperatures below  $T_{\text{CMB}}$ . These are the sight lines to HD 73882, where  $T_{01} = 2.631 \pm 0.004$  K (3.4% below  $T_{\text{CMB}}$ ), and HD 210121, for which  $T_{01} = 2.604 \pm 0.007$  K (4.4% below  $T_{\text{CMB}}$ ). The rotational excitation temperatures in the other two directions with strong CN are significantly above  $T_{\text{CMB}}$ . For HD 154368, we find  $T_{01} = 2.911 \pm 0.004$  K (6.8% above  $T_{\text{CMB}}$ ), while for the sight line to HD 169454, we obtain  $T_{01} = 2.804 \pm 0.003$  K (2.9% above  $T_{\text{CMB}}$ ). Since there is no known physical mechanism that can lower  $T_{01}$  below the temperature of the cosmic microwave background, our results for HD 73882 and HD 210121 indicate that perhaps the uncertainties have been underestimated in these instances. The sight lines to HD 73882, HD 154368,

HD 169454, and HD 210121 exhibit the largest CN optical depths in our sample, meaning that the excitation temperatures are sensitive to small changes in  $b$ . Increases in  $b$  of only  $0.03 \text{ km s}^{-1}$  and  $0.06 \text{ km s}^{-1}$  for HD 73882 and HD 210121, respectively, would be sufficient to bring the derived values of  $T_{01}$  into agreement with  $T_{\text{CMB}}$ . (Likewise, for HD 154368 and HD 169454, decreases in  $b$  of  $0.04 \text{ km s}^{-1}$  and  $0.01 \text{ km s}^{-1}$ , respectively, would eliminate the small excesses in  $T_{01}$  observed in these directions.) Such small changes would not be unreasonable considering the level of variation present in the  $b$ -values obtained through the doublet ratio method for these sight lines (see Table 5).

Figure 20 plots our derived CN excitation temperatures for individual velocity components (shown as  $3\text{-}\sigma$  error bars) against the CN/CH<sup>+</sup> column density ratio, an empirical density indicator (see Sheffer et al. 2008). The CMB temperature ( $2.725 \pm 0.002 \text{ K}$ ; Mather et al. 1999) and our weighted mean value ( $2.754 \pm 0.002 \text{ K}$ ) are indicated in the figure. Also shown are the (unweighted) mean and standard deviation for our sample of excitation temperatures ( $2.707 \pm 0.134 \text{ K}$ ). In all but two cases, the derived values of  $T_{01}$  are within one standard deviation of the unweighted mean, even if the individual errors are much smaller. (The small error bars at high density that are below  $T_{\text{CMB}}$  are for the sight lines to HD 73882 and HD 210121 discussed above.) Only in the main component toward HD 154368 and in the  $-3.1 \text{ km s}^{-1}$  component toward HD 161056 is  $T_{01}$  more than  $134 \text{ mK}$  larger than the average and both of these clouds have high CN/CH<sup>+</sup> ratios. For the latter component, we find  $T_{01} = 2.960 \pm 0.018 \text{ K}$ . This result may be particularly significant since the CN column densities toward HD 161056 seem not to be affected by optical depth effects in any appreciable way. Additionally, the excitation temperature in the  $+2.8 \text{ km s}^{-1}$  component in this direction ( $T_{01} = 2.761 \pm 0.020 \text{ K}$ ) is consistent with  $T_{\text{CMB}}$  at the  $2\text{-}\sigma$  level and this component has a CN/CH<sup>+</sup> ratio that is a factor 30 lower than the ratio in the  $-3.1 \text{ km s}^{-1}$  component. A rotational temperature in excess of  $T_{\text{CMB}}$  results from a local excitation mechanism, presumably electron impact (Thaddeus 1972). As such, an excess in  $T_{01}$  might be expected at higher gas densities, if the electron density in the gas is also higher.

To further explore the local excitation process, we can use our determinations of  $T_{01}$  to derive estimates for the electron density  $n_e$  in these clouds. Our approach differs from previous analyses of this kind (e.g., Meyer & Jura 1985; Palazzi et al. 1992; Roth & Meyer 1995) in that past investigators have used an independent measure of the contribution to  $T_{01}$  from local collisional excitation,  $T_{\text{loc}}$ , to correct their  $T_{01}$  values in order to derive the temperature of the CMB. These studies have estimated the local contribution either from ionization balance by using column densities of Ca I and Ca II, for example, to calculate  $n_e$ , or from microwave observations of CN emission at  $2.64 \text{ mm}$  to evaluate  $T_{\text{loc}}$  directly. In our analysis, we adopt  $T_{\text{CMB}} = 2.725 \text{ K}$ , and assume that any additional excitation results from electron collisions. The excess temperature, then, yields an estimate for the electron density in the gas. Following Thaddeus (1972), the rate of excitation from  $N = 0$  to  $N = 1$  may be written

$$\begin{aligned} C_{01} &= \left(\frac{g_1}{g_0}\right) A_1 \exp\left(-\frac{h\nu}{k_B T_{01}}\right) \left[1 - \exp\left(-\frac{h\nu}{k_B T_{01}}\right)\right]^{-1} \\ &= \left(\frac{g_1}{g_0}\right) A_1 \left[\exp\left(\frac{h\nu}{k_B T_{01}}\right) - 1\right]^{-1}, \end{aligned} \quad (7)$$

where  $A_1 = 1.19 \times 10^{-5} \text{ s}^{-1}$  (Thaddeus 1972) is the spontaneous radiative decay rate of the  $N = 1$  level and  $C_{01}$  represents the total rate, including both radiative and collisional excitation. If  $T_{01} = T_{\text{CMB}}$ , then the excitation rate is  $C_{01} = C_{\text{CMB}} = 5.60 \times 10^{-6} \text{ s}^{-1}$ . Any local excitation will increase this rate. Thus, when  $T_{01} > T_{\text{CMB}}$ , the local rate is given by  $C_{\text{loc}} = C_{01} - C_{\text{CMB}}$ . Once  $C_{\text{loc}}$  is known, the electron density can be found from  $n_e = C_{\text{loc}}/r_{01}$ , where  $r_{01}$  is the rate coefficient for CN rotational excitation by electron impact.

We calculated  $n_e$  from equation (7) and the above relations for clouds with significant excesses in  $T_{01}$  by assuming a gas kinetic temperature of  $20 \text{ K}$ . This temperature corresponds to that calculated by Sonnentrucker et al. (2007) for the clouds toward HD 154368 and HD 169454 from their analysis of C<sub>2</sub> rotational excitation. The rate coefficient given by Allison & Dalgarno (1971) for CN excitation by electron impact at  $T_{\text{kin}} = 20 \text{ K}$  is  $r_{01} = 1.3 \times 10^{-6} \text{ cm}^3 \text{ s}^{-1}$ . For the main component toward HD 154368, which has an excess rotational temperature of  $186 \text{ mK}$ , these calculations yield an electron density of  $0.69 \text{ cm}^{-3}$ . For the  $-3.1 \text{ km s}^{-1}$  component toward HD 161056, where the measured excess is  $235 \text{ mK}$ , we find  $n_e = 0.88 \text{ cm}^{-3}$ . Finally, for HD 169454, the excess of  $79 \text{ mK}$  gives  $n_e = 0.29 \text{ cm}^{-3}$ . These electron densities are generally larger than those derived by Black & van Dishoeck (1991), who found values of  $n_e$  in the range  $0.02\text{--}0.5 \text{ cm}^{-3}$ , and would indicate large gas densities in the cloud cores ( $n_{\text{H}} \sim 6000 \text{ cm}^{-3}$  for the component at  $-3.1 \text{ km s}^{-1}$  toward HD 161056, assuming  $n_e/n_{\text{H}} \sim 1.4 \times 10^{-4}$ ). The problem is even more severe in cases where  $f(\text{CO})$  is substantial [e.g., toward HD 154368, where we find  $f(\text{CO}) \sim 0.5$ ], since fewer carbon atoms are available to provide free electrons. For comparison, Sonnentrucker et al. (2007) find  $n_{\text{H}} \sim 250 \text{ cm}^{-3}$  for HD 154368 and HD 169454 based on their C<sub>2</sub> analysis, while Sheffer et al. (2008) obtain  $n_{\text{H}} \sim 750 \text{ cm}^{-3}$  for the main component toward HD 154368 using an analytical expression involving the formation and destruction pathways for CN.

It is probably more appropriate to consider the electron densities derived from the excess rotational temperatures in CN to be upper limits because excitation from neutral impacts (mainly H<sub>2</sub>) can also contribute. Moreover, the actual excess temperature due to local collisional excitation is likely to be less than the measured value of  $T_{\text{loc}} = T_{01} - T_{\text{CMB}}$ , considering the dispersion of  $134 \text{ mK}$  in our determinations of  $T_{01}$ . Taking this dispersion into account, the actual excess temperatures for the clouds toward HD 154368 and HD 161056 might be as low as  $52 \text{ mK}$  and  $101 \text{ mK}$ , respectively. Indeed, from observations of CN emission at  $2.64 \text{ mm}$ , Palazzi et al. (1990) find  $T_{\text{loc}} = 35 \pm 9 \text{ mK}$  for the main component toward HD 154368. These lower excesses would yield electron densities of  $n_e = 0.19 \text{ cm}^{-3}$  for HD 154368 and  $0.37 \text{ cm}^{-3}$  for the  $-3.1 \text{ km s}^{-1}$  component toward HD 161056. An

excess in  $T_{01}$  would then not be inferred for HD 169454, since the observed rotational temperature in this direction is within the typical dispersion of the sample. Here, again, we see a need for improved detailed models, in this case, of the excitation processes in diffuse molecular clouds. The precise set of observational results presented in this work would offer robust constraints for any such modeling efforts.

## 6. CONCLUDING REMARKS

Isotopologic ratios in interstellar molecules containing carbon are effective probes of the chemical processes active in diffuse environments. In this investigation, we examined optical absorption lines of CN and CH<sup>+</sup> along a total of thirteen lines of sight through diffuse molecular clouds. The very high signal-to-noise ratio observations enabled us to extract precise  $^{12}\text{CN}/^{13}\text{CN}$  and  $^{12}\text{CH}^+ / ^{13}\text{CH}^+$  ratios, which were used to assess various predictions of diffuse cloud chemistry.

Our results on  $^{12}\text{CH}^+ / ^{13}\text{CH}^+$  confirm that this ratio does not deviate from the ambient  $^{12}\text{C}/^{13}\text{C}$  ratio in local interstellar clouds, as expected if CH<sup>+</sup> is formed via nonthermal processes. Each of the McDonald sight lines in our sample with detectable absorption from  $^{13}\text{CH}^+$  had at one time been found to have either a much lower or a much higher value of  $^{12}\text{CH}^+ / ^{13}\text{CH}^+$ . Such values are not confirmed here. In particular, the  $^{12}\text{CH}^+ / ^{13}\text{CH}^+$  ratios that we derive toward the Pleiades stars, 20 Tau and 23 Tau, are both indistinguishable from 70, precluding a  $^{12}\text{C}/^{13}\text{C}$  ratio near 40, as advocated by Hawkins & Jura (1987), for the gas associated with this nearby cluster. Considering these results, we find no evidence for variation in  $^{12}\text{C}/^{13}\text{C}$  within the solar neighborhood. In contrast, the studies by Casassus et al. (2005) and Stahl et al. (2008), based on UVES spectra, found variation in  $^{12}\text{CH}^+ / ^{13}\text{CH}^+$  at about the 16% level. These authors attributed the variation to intrinsic scatter in the local  $^{12}\text{C}/^{13}\text{C}$  ratio due to inefficient or incomplete mixing in the interstellar medium. From our analysis of some of the same UVES data, we conclude that the variation in  $^{12}\text{CH}^+ / ^{13}\text{CH}^+$  is likely related to the difficulties of obtaining accurate  $^{12}\text{CH}^+ / ^{13}\text{CH}^+$  ratios from these spectra. The major difficulties involve the placement of the rather poorly-defined continua, and the blending of absorption from  $^{13}\text{CH}^+$  with weak  $^{12}\text{CH}^+$  components blueward of the main components. It is probably not a coincidence that the  $^{12}\text{CH}^+ / ^{13}\text{CH}^+$  ratios derived from our high-resolution McDonald spectra, which have flat, well-behaved continua, along lines of sight with simple CH<sup>+</sup> absorption profiles show little variation. While intrinsic scatter in the local  $^{12}\text{C}/^{13}\text{C}$  ratio may exist at some level, due to small differences in the amount of chemical enrichment and subsequent mixing from one site to another, it is probably too early to say that this variation has been detected.

Unlike in the case of CH<sup>+</sup>, the isotopologic ratios in CN and CO show evidence for significant fractionation away from the ambient value of  $^{12}\text{C}/^{13}\text{C}$  in some diffuse environments. We attribute these results to the competing influences of isotope-selective photodissociation and isotopic charge exchange reactions, which vary with the strength of the UV radiation field and the physical conditions within a cloud. The results on  $^{12}\text{CN}/^{13}\text{CN}$  and  $^{12}\text{CO}/^{13}\text{CO}$  in lines of sight where both ratios have

been determined are suggestive of the inverse relationship between these quantities that is anticipated, assuming that CN and CO coexist in diffuse cloud cores. This relationship was first directly suggested by Sheffer et al. (2007), but the isotopologic results for CN that existed at the time were not extensive enough to adequately test the idea. With the results presented here, the situation is now significantly improved, but further observations of both  $^{12}\text{CN}/^{13}\text{CN}$  and  $^{12}\text{CO}/^{13}\text{CO}$  would help to clarify the precise relationship between the two quantities. Specifically, measurements of  $^{12}\text{CO}/^{13}\text{CO}$  toward HD 169454, where  $^{12}\text{CN}/^{13}\text{CN}$  is unfractionated, and toward HD 170740, where CN is fractionated upward (by a factor of  $1.9 \pm 0.5$  over the ambient value), would prove useful. One aspect of the chemistry of diffuse clouds that future modeling efforts will need to examine is the role played by isotopic charge exchange with CN, which we have found to be important in cold diffuse cloud cores. An ICE reaction involving CN is the most logical explanation for why the enhancements in  $^{12}\text{CN}/^{13}\text{CN}$  are not as large as expected along lines of sight with low  $^{12}\text{CO}/^{13}\text{CO}$  ratios, such as HD 73882 and HD 154368.

The effects of photochemical fractionation in carbon-bearing molecules are predicted to be the strongest in diffuse molecular clouds because dark clouds are better shielded from UV radiation and lack a significant abundance of carbon ions. This has been convincingly demonstrated by millimeter-wave emission studies of CN, CO, and H<sub>2</sub>CO (see Milam et al. 2005). However, it is interesting to note that the expression developed in § 4.3, which yields the fraction of carbon locked up in CO, may still apply in denser regions. Keene et al. (1998) detected 809 GHz emission from both  $^{12}\text{C}^0$  and  $^{13}\text{C}^0$  near the center of the Orion Nebula, finding a  $^{12}\text{C}^0 / ^{13}\text{C}^0$  ratio of  $58 \pm 12$ . This was after Boreiko & Betz (1996) observed 158  $\mu\text{m}$  emission from both isotopic variants of C<sup>+</sup> in this region and found a  $^{12}\text{C}^+ / ^{13}\text{C}^+$  ratio of  $58 \pm 6$ . The  $^{12}\text{C}^{18}\text{O} / ^{13}\text{C}^{18}\text{O}$  ratio, also derived by Keene et al. (1998) from observations of the 2–1 and 3–2 transitions, is  $75 \pm 9$ . While all of these ratios are consistent with an ambient  $^{12}\text{C}/^{13}\text{C}$  ratio of 70, the exact correspondence between the ratios in neutral and ionized carbon suggests that there is a real difference between those ratios and that found in C<sup>18</sup>O. Since these observations sample gas in a well-known photon-dominated region (PDR), it is reasonable to assume that the slight increase in the  $^{12}\text{C}^{18}\text{O} / ^{13}\text{C}^{18}\text{O}$  ratio over the ambient value is the result of selective photodissociation. An application of equation (2) to these measurements, with the substitution of  $f(^{13}\text{C}^+)$  for  $f(^{13}\text{CN})$ , would yield a value of  $f(\text{CO}) = 0.76$ , which is consistent with expectations for gas in a dense molecular cloud like that in Orion. We contrast this result with the values of  $f(\text{CO})$  we obtain toward the diffuse molecular clouds in Ophiuchus, namely 0.40 toward  $\rho$  Oph A and 0.45 toward  $\zeta$  Oph. The Ophiuchus results are appropriate for sight lines that probe the transition region between diffuse and dense clouds, where the conversion of C<sup>+</sup> into CO is expected to occur.

Beyond isotopologic ratios, the high quality optical spectra examined in this investigation allowed us to obtain precise rotational excitation temperatures for both  $^{12}\text{CN}$  and  $^{13}\text{CN}$ . Our weighted mean value of  $T_{01}(^{12}\text{CN}) = 2.754 \pm 0.002$  K implies an excess over the temperature of the cosmic microwave background of only  $29 \pm 3$  mK.

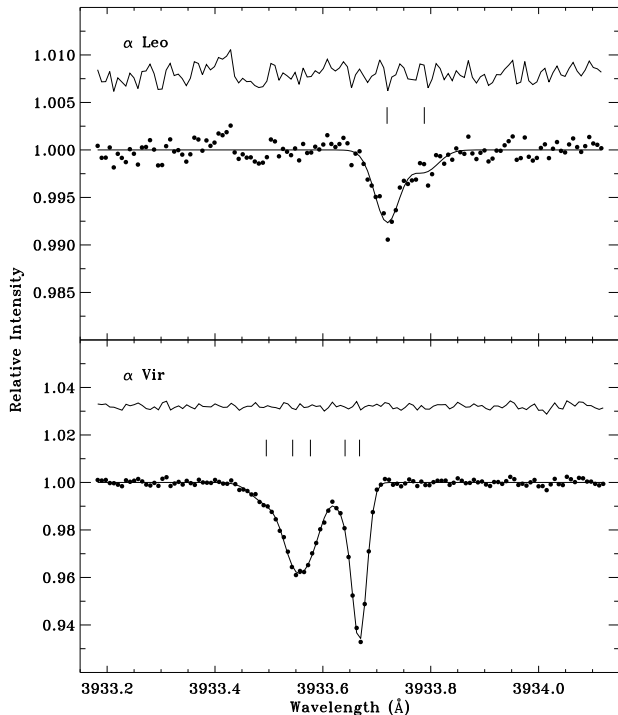


**Figure 21.** Synthetic fits to the Ca II K profiles toward the unreddened stars  $\alpha$  Leo (*upper panel*) and  $\alpha$  Vir (*lower panel*). Plotting symbols are the same as in Figure 3. The Ca II profile in the direction of  $\alpha$  Leo is synthesized using two line-of-sight components, with LSR velocities of  $+4.4$  and  $+9.7$  km  $s^{-1}$ . For  $\alpha$  Vir, five components comprise the fit. These have LSR velocities of  $-12.7$ ,  $-8.9$ ,  $-6.4$ ,  $-1.5$ , and  $+0.5$  km  $s^{-1}$ .

This excess is considerably smaller than that suggested in the recent survey by Slyk et al. (2008), but is also reduced compared to the excess found by Palazzi et al. (1992). Both of these previous studies indicated the need for an additional excitation mechanism beyond electron and neutral collisions (and the CMB) to account for the observed excitation of CN. The more modest excess found here eliminates the need for such a mechanism in the general ISM. Only three sight lines in our sample exhibit significant excesses in  $T_{01}$  over the cosmic microwave background temperature. For the clouds in these directions, we derived upper limits to the electron densities in the range  $0.3$ – $0.9$   $cm^{-3}$ . The rotational excitation temperatures observed in  $^{13}CN$ , from strong detections of the  $R(0)$  and  $R(1)$  lines in four directions and the first interstellar detection of the  $P(1)$  line, show no excess over the temperature of the CMB.

We are grateful to Yaron Sheffer for allowing us the use of his program ISMOD and to Dan Welty for suggesting that we include the VLT sight lines in our analysis. D. L. L. thanks the Robert A. Welch Foundation for support through grant F-634. This research made use of the ESO Science Archive Facility as well as the SIMBAD database operated at CDS, France.

## APPENDIX

### INTERSTELLAR ABSORPTION TOWARD UNREDDENED STARS

In this appendix, we provide results on weak Ca I

( $\lambda 4226$ ) and Ca II K ( $\lambda 3933$ ) absorption toward the stars  $\alpha$  Leo and  $\alpha$  Vir, which served as unreddened standard stars for our McDonald observations. Although  $\alpha$  Lyr was also observed once as a standard, strong stellar lines in the vicinity of Ca I and Ca II K, as well as lower S/N, prevent any interstellar features from being discerned in this direction. Table 10 presents the equivalent widths of Ca I and Ca II K for the other two stars along with previous measurements and upper limits from the literature. Figure 21 shows our fits to the observed Ca II K profiles. For  $\alpha$  Leo, the fit results in a total column density of  $N(\text{Ca II}) = (0.69 \pm 0.08) \times 10^{10}$   $cm^{-2}$ . A similar fit to the Ca I profile yields a column density of  $N(\text{Ca I}) = (0.42 \pm 0.11) \times 10^9$   $cm^{-2}$ . For  $\alpha$  Vir, our Ca II K profile synthesis fit gives  $N(\text{Ca II}) = (7.11 \pm 0.15) \times 10^{10}$   $cm^{-2}$ . No Ca I absorption is detected in the direction of  $\alpha$  Vir, but we derive an upper limit on the column density of  $N(\text{Ca I}) \lesssim 0.21 \times 10^9$   $cm^{-2}$ .

## REFERENCES

- Allison, A. C., & Dalgarno, A. 1971, *A&A*, 13, 331  
 Bakker, E. J., & Lambert, D. L. 1998, *ApJ*, 502, 417  
 Bembek, Z. 1997, *J. Mol. Spectrosc.*, 181, 136  
 Black, J. H., & van Dishoeck, E. F. 1988, *ApJ*, 331, 986  
 Black, J. H., & van Dishoeck, E. F. 1991, *ApJ*, 369, L9  
 Boreiko, R. T., & Betz, A. L. 1996, *ApJ*, 467, L113  
 Burgh, E. B., France, K., & McCandliss, S. R. 2007, *ApJ*, 658, 446  
 Carrington, A., & Ramsay, D. A. 1982, *Phys. Scr.*, 25, 272  
 Casassus, S., Stahl, O., & Wilson, T. L. 2005, *A&A*, 441, 181  
 Centurión, M., & Vladilo, G. 1991, *A&A*, 251, 245  
 Centurión, M., Càssola, C., & Vladilo, G. 1995, *A&A*, 302, 243  
 Crane, P., & Hegyi, D. J. 1988, *ApJ*, 326, L35  
 Crane, P., Hegyi, D. J., Kutner, M. L., & Mandolesi, N. 1989, *ApJ*, 346, 136  
 Crane, P., Hegyi, D. J., & Lambert, D. L. 1991, *ApJ*, 378, 181  
 Crane, P., Hegyi, D. J., Mandolesi, N., & Danks, A. C. 1986, *ApJ*, 309, 822  
 de Vries, C. P., & van Dishoeck, E. F. 1988, *A&A*, 203, L23  
 Elitzur, M., & Watson, W. D. 1978, *ApJ*, 222, L141  
 Elitzur, M., & Watson, W. D. 1980, *ApJ*, 236, 172  
 Federman, S. R., Danks, A. C., & Lambert, D. L. 1984, *ApJ*, 287, 219  
 Federman, S. R., Lambert, D. L., Sheffer, Y., Cardelli, J. A., Andersson, B.-G., van Dishoeck, E. F., & Žsargó, J. 2003, *ApJ*, 591, 986  
 Federman, S. R., Strom, C. J., Lambert, D. L., Cardelli, J. A., Smith, V. V., & Joseph, C. L. 1994, *ApJ*, 424, 772  
 Fixsen, D. J. 2009, *ApJ*, 707, 916  
 Gredel, R., van Dishoeck, E. F., & Black, J. H. 1991, *A&A*, 251, 625  
 Gredel, R., van Dishoeck, E. F., & Black, J. H. 1993, *A&A*, 269, 477  
 Hanson, M. M., Snow, T. P., & Black, J. H. 1992, *ApJ*, 392, 571  
 Hawkins, I., Craig, N., & Meyer, D. M. 1993, *ApJ*, 407, 185  
 Hawkins, I., & Jura, M. 1987, *ApJ*, 317, 926  
 Hawkins, I., Jura, M., & Meyer, D. M. 1985, *ApJ*, 294, L131  
 Hawkins, I., Jura, M., Meyer, D. M., & Craig, N. 1989, *BAAS*, 21, 1142  
 Henkel, C., Wilson, T. L., & Bieging, J. 1982, *A&A*, 109, 344  
 Hobbs, L. M. 1975, *ApJ*, 202, 628  
 Hobbs, L. M. 1978, *ApJ*, 222, 491  
 Hoffleit, D., & Jaschek, C. 1982, *The Bright Star Catalogue* (4th ed.; New Haven: Yale University Observatory)  
 Jenkins, E. B., Drake, J. F., Morton, D. C., Rogerson, J. B., Spitzer, L., & York, D. G. 1973, *ApJ*, 181, L122  
 Kaiser, M. E., Hawkins, I., & Wright, E. L. 1991, *ApJ*, 379, 267  
 Kaiser, M. E., & Wright, E. L. 1990, *ApJ*, 356, L1  
 Keene, J., Schilke, P., Kooi, J., Lis, D. C., Mehringer, D. M., & Phillips, T. G. 1998, *ApJ*, 494, L107  
 Knauth, D. C., Federman, S. R., Pan, K., Yan, M., & Lambert, D. L. 2001, *ApJS*, 135, 201  
 Lallement, R., Vidal-Madjar, A., & Ferlet, R. 1986, *A&A*, 168, 225  
 Lambert, D. L., Sheffer, Y., & Crane, P. 1990, *ApJ*, 359, L19  
 Lambert, D. L., Sheffer, Y., Gilliland, R. L., & Federman, S. R. 1994, *ApJ*, 420, 756  
 Langer, W. D., & Penzias, A. A. 1990, *ApJ*, 357, 477  
 Lodders, K. 2003, *ApJ*, 591, 1220

- Mather, J. C., Fixsen, D. J., Shafer, R. A., Mosier, C., & Wilkinson, D. T. 1999, *ApJ*, 512, 511
- Meyer, D. M., & Jura, M. 1985, *ApJ*, 297, 119
- Meyer, D. M., Roth, K. C., & Hawkins, I. 1989, *ApJ*, 343, L1
- Milam, S. N., Savage, C., Brewster, M. A., Ziurys, L. M., & Wyckoff, S. 2005, *ApJ*, 634, 1126
- Palazzi, E., Mandolesi, N., Crane, P., Kutner, M. L., Blades, J. C., & Hegyi, D. J. 1990, *ApJ*, 357, 14
- Palazzi, E., Mandolesi, N., & Crane, P. 1992, *ApJ*, 398, 53
- Pan, K., Federman, S. R., Cunha, K., Smith, V. V., & Welty, D. E. 2004, *ApJS*, 151, 313
- Pan, K., Federman, S. R., Sheffer, Y., & Andersson, B.-G. 2005, *ApJ*, 633, 986
- Perryman, M. A. C., et al. 1997, *A&A*, 323, L49
- Prasad, C. V. V., Bernath, P. F., Frum, C., & Engleman, R., Jr. 1992, *J. Mol. Spectrosc.*, 151, 459
- Rachford, B. L., et al. 2002, *ApJ*, 577, 221
- Rachford, B. L., et al. 2009, *ApJS*, 180, 125
- Ritchey, A. M., Martinez, M., Pan, K., Federman, S. R., & Lambert, D. L. 2006, *ApJ*, 649, 788
- Roth, K. C., & Meyer, D. M. 1995, *ApJ*, 441, 129
- Savage, C., Apponi, A. J., Ziurys, L. M., & Wyckoff, S. 2002, *ApJ*, 578, 211
- Sheffer, Y., Federman, S. R., Lambert, D. L., & Cardelli, J. A. 1992, *ApJ*, 397, 482
- Sheffer, Y., Lambert, D. L., & Federman, S. R. 2002, *ApJ*, 574, L171
- Sheffer, Y., Rogers, M., Federman, S. R., Abel, N. P., Gredel, R., Lambert, D. L., & Shaw, G. 2008, *ApJ*, 687, 1075
- Sheffer, Y., Rogers, M., Federman, S. R., Lambert, D. L., & Gredel, R. 2007, *ApJ*, 667, 1002
- Slyk, K., Bondar, A. V., Galazutdinov, G. A., & Krelowski, J. 2008, *MNRAS*, 390, 1733
- Sonnentrucker, P., Welty, D. E., Thorburn, J. A., & York, D. G. 2007, *ApJS*, 168, 58
- Spitzer, L. 1978, *Physical Processes in the Interstellar Medium* (New York: Wiley)
- Stahl, O., Casassus, S., & Wilson, T. 2008, *A&A*, 477, 865
- Stahl, O., & Wilson, T. L. 1992, *A&A*, 254, 327
- Stahl, O., Wilson, T. L., Henkel, C., & Appenzeller, I. 1989, *A&A*, 221, 321
- Thaddeus, P. 1972, *ARA&A*, 10, 305
- Tull, R. G., Macqueen, P. J., Sneden, C., & Lambert, D. L. 1995, *PASP*, 107, 251
- Valencic, L. A., Clayton, G. C., & Gordon, K. D. 2004, *ApJ*, 616, 912
- Vallerga, J. V., Vedder, P. W., Craig, N., & Welsh, B. Y. 1993, *ApJ*, 411, 729
- Vanden Bout, P. A., & Snell, R. L. 1980, *ApJ*, 236, 460
- van Dishoeck, E. F., & Black, J. H. 1988, *ApJ*, 334, 771
- Visser, R., van Dishoeck, E. F., & Black, J. H. 2009, *A&A*, 503, 323
- Vladilo, G., Centurión, M., & Càssola, C. 1993, *A&A*, 273, 239
- Watson, W. D., Anicich, V. G., & Huntress, W. T., Jr. 1976, *ApJ*, 205, L165
- Wegner, W. 2003, *Astron. Nachr.*, 324, 219
- Welty, D. E., & Fowler, J. R. 1992, *ApJ*, 393, 193
- Welty, D. E., Hobbs, L. M., & Morton, D. C. 2003, *ApJS*, 147, 61
- Welty, D. E., Morton, D. C., & Hobbs, L. M. 1996, *ApJS*, 106, 533
- White, R. E., Allen, C. L., Forrester, W. B., Gonnella, A. M., & Young, K. L. 2001, *ApJS*, 132, 253
- Wilson, T. L. 1999, *Rep. Prog. Phys.*, 62, 143
- Wilson, T. L., & Rood, R. 1994, *ARA&A*, 32, 191

**Table 1**  
Stellar and Observational Data

Star	Name	Sp. Type	$B$ (mag)	$E(B - V)$ (mag)	Ref.	$l$ (deg)	$b$ (deg)	$d^a$ (pc)	Exp. Time <sup>b</sup> (hr)	S/N <sup>b</sup>
McDonald Sight Lines										
HD 23408	20 Tau	B7 III	3.81	0.07	1	166.17	-23.51	110 ± 13	15.5/14.5	610/1240
HD 23480	23 Tau	B6 IV	4.11	0.10	1	166.57	-23.75	110 ± 13	33.0/33.0	1180/1930
HD 24398	ζ Per	B1 Ib	2.97	0.34	2	162.29	-16.69	301 ± 68	6.6/6.4	810/1500
HD 147933	ρ Oph A	B2 V	5.26	0.45	3	353.69	+17.69	90	43.9/42.4	1100/1600
HD 149757	ζ Oph	O9.5 V	2.60	0.32	3	6.28	+23.59	140 ± 14	7.5/7.5	650/1590
HD 179406	20 Aql	B3 V	5.45	0.33	4	28.23	-8.31	160	22.3/22.8	900/1230
VLT/UVES Sight Lines										
HD 73882	NX Vel	O8.5 Vn	7.58	0.70	4	260.18	+0.64	820	1.7	1320
HD 152236	ζ <sup>1</sup> Sco	B1 Ia+pe	5.18	0.68	4	343.03	+0.87	600	0.2	1090
HD 154368	V1074 Sco	O9.5 Iab	6.57	0.78	4	349.97	+3.22	1100	2.7	1680
HD 161056		B1.5 V	6.68	0.59	2	18.67	+11.58	280	3.1	1480
HD 169454	V430 Sct	B1 Ia	7.39	1.08	3	17.54	-0.67	750	6.4	1990
HD 170740		B2 V	5.93	0.48	4	21.06	-0.53	213 ± 43	2.2	1590
HD 210121		B9 V	7.83	0.31	3	56.88	-44.46	210 ± 45	1.3	1160

**References.** — (1) White et al. 2001; (2) Wegner 2003; (3) Valencic et al. 2004; (4) Rachford et al. 2009.

<sup>a</sup> Distances with error bars are from  $\geq 4\text{-}\sigma$  *Hipparcos* results. Other distances are derived by means of spectroscopic parallax.

<sup>b</sup> Exposure time and signal-to-noise ratio per resolution element for spectral region near CN  $\lambda 3874/\text{CH}^+ \lambda 4232$ . For the VLT/UVES sight lines, the values refer to the CN  $\lambda 3874$  region.

**Table 2**  
Comparison of Total Equivalent Widths for  $\text{CH}^+$   
 $\lambda 4232$

Star	$W_\lambda(^{12}\text{CH}^+)$ (mÅ)	$W_\lambda(^{13}\text{CH}^+)$ (mÅ)	Ref.
20 Tau	24.93 ± 0.07	0.36 ± 0.07	1
	23.3 ± 0.3	0.67 ± 0.15	2
	23.5	0.57 ± 0.11	3
23 Tau	15.19 ± 0.05	0.23 ± 0.05	1
	14.94 ± 0.02	0.15	4
	14.0 ± 0.2	0.36 ± 0.08	2
ρ Oph A	12.50 ± 0.06	0.21 ± 0.06	1
	12.25 ± 0.09	0.11 ± 0.05	5
ζ Oph	23.00 ± 0.06	0.36 ± 0.06	1
	23.42 ± 0.03	0.29	6
	23.8 ± 0.09	0.45 ± 0.06	7
	23.25 ± 0.07	0.41 ± 0.02	8
	22.62 ± 0.04	0.34 ± 0.01	9
	22.5 ± 0.2	0.54 ± 0.1	10
	21.7 ± 0.2	0.59 ± 0.10	11
23.5	0.36 ± 0.06	3	

**References.** — (1) This Work; (2) Hawkins & Jura 1987; (3) Vanden Bout & Snell 1980; (4) Stahl et al. 2008; (5) Federman et al. 2003; (6) Casassus et al. 2005; (7) Hawkins et al. 1993; (8) Crane et al. 1991; (9) Stahl et al. 1989; (10) Hawkins et al. 1989; (11) Hawkins et al. 1985.

**Table 3**  
Comparison of Total Equivalent Widths for CN  $\lambda$ 3874

Star	<sup>12</sup> CN			<sup>13</sup> CN		Ref.
	$W_\lambda R(0)$ (mÅ)	$W_\lambda R(1)$ (mÅ)	$W_\lambda P(1)$ (mÅ)	$W_\lambda R(0)$ (mÅ)	$W_\lambda R(1)$ (mÅ)	
McDonald Sight Lines						
$\zeta$ Per	$8.88 \pm 0.06$	$2.72 \pm 0.06$	$1.36 \pm 0.06$	$0.16 \pm 0.06$	...	1
	$8.70 \pm 0.6$	$2.64 \pm 0.2$	$1.00 \pm 0.3$	...	...	2
	$9.06 \pm 0.17$	$2.79 \pm 0.17$	$1.36 \pm 0.17$	...	...	3
	$8.4 \pm 0.21$	...	...	$0.12 \pm 0.02$	...	4
	$8.99 \pm 0.02$	$2.89 \pm 0.02$	$1.30 \pm 0.02$	...	...	5
	$8.06 \pm 0.07$	$2.51 \pm 0.04$	$1.28 \pm 0.04$	...	...	6
$\rho$ Oph A	$6.12 \pm 0.04$	$1.95 \pm 0.04$	$0.95 \pm 0.04$	$0.15 \pm 0.04$	...	1
	$6.53 \pm 0.4$	$2.18 \pm 0.4$	$1.33 \pm 0.4$	...	...	2
	$6.1 \pm 0.4$	$1.9 \pm 0.3$	$1.1 \pm 0.3$	...	...	7
	$6.11 \pm 0.48$	$2.08 \pm 0.67$	$1.05 \pm 0.59$	...	...	8
	$5.9 \pm 0.3$	$2.5 \pm 0.3$	$1.2 \pm 0.7$	...	...	9
$\zeta$ Oph	$7.98 \pm 0.08$	$2.37 \pm 0.08$	$1.27 \pm 0.08$	$0.19 \pm 0.08$	...	1
	$8.31 \pm 0.3$	$2.56 \pm 0.4$	$1.29 \pm 0.6$	...	...	2
	$8.17 \pm 0.04$	$2.50 \pm 0.04$	$1.29 \pm 0.04$	$0.27 \pm 0.10$	...	3
	$8.16 \pm 0.03$	...	...	$0.10 \pm 0.05$	...	10
	$7.75 \pm 0.04$	$2.45 \pm 0.02$	$1.26 \pm 0.02$	$0.19 \pm 0.02$	...	11, 12
	$7.34 \pm 0.12$	$2.13 \pm 0.06$	$1.08 \pm 0.07$	...	...	6
20 Aql	$10.92 \pm 0.07$	$3.29 \pm 0.07$	$1.64 \pm 0.07$	$0.20 \pm 0.07$	...	1
	$11.16 \pm 0.2$	$3.99 \pm 0.2$	$1.86 \pm 0.2$	...	...	2
	$11.5 \pm 0.2$	$3.2 \pm 0.2$	$1.6 \pm 0.2$	...	...	13
VLT/UVES Sight Lines						
HD 73882	$34.01 \pm 0.06$	$19.72 \pm 0.06$	$12.07 \pm 0.06$	$1.44 \pm 0.06$	$0.39 \pm 0.06$	1
	$34.83 \pm 1.93$	$17.31 \pm 0.55$	$10.23 \pm 0.42$	...	...	8
	$31.8 \pm 0.7$	$20.2 \pm 1.3$	$13.7 \pm 1.2$	$0.7 \pm 0.5$	...	14
HD 152236 (+6.0) <sup>a</sup>	$7.09 \pm 0.06$	$2.22 \pm 0.06$	$1.20 \pm 0.06$	$0.13 \pm 0.06$	...	1
	$6.09 \pm 0.32$	$2.09 \pm 0.60$	$0.74 \pm 0.59$	...	...	8
HD 154368 (+5.2) <sup>a</sup>	$25.30 \pm 0.04$	$15.59 \pm 0.04$	$9.66 \pm 0.04$	$1.13 \pm 0.04$	$0.33 \pm 0.04$	1
	$26.58 \pm 0.6$	$15.19 \pm 0.7$	$10.01 \pm 0.2$	...	...	2
	$25.34 \pm 0.23$	$14.85 \pm 0.22$	$9.21 \pm 0.23$	...	...	3
	$22.5 \pm 2.8$	$16.8 \pm 2.3$	$8.1 \pm 0.9$	...	...	14
	$24.62 \pm 0.13$	$15.12 \pm 0.11$	$9.74 \pm 0.09$	$0.82 \pm 0.10$	$0.25 \pm 0.08$	15
HD 161056 (−3.1)	$12.23 \pm 0.05$	$4.49 \pm 0.05$	$2.33 \pm 0.05$	$0.41 \pm 0.05$	...	1
	$11.47 \pm 0.6$	$3.38 \pm 0.6$	...	...	...	2
	$8.7 \pm 1.0$	$1.1 \pm 1.0$	$2.0 \pm 1.0$	...	...	14
HD 161056 (+2.8)	$14.15 \pm 0.06$	$4.26 \pm 0.06$	$2.22 \pm 0.06$	$0.43 \pm 0.06$	...	1
	$15.51 \pm 0.6$	$4.54 \pm 0.6$	...	...	...	2
	$15.6 \pm 1.0$	$4.7 \pm 1.0$	$3.0 \pm 1.0$	...	...	14
HD 169454	$22.22 \pm 0.04$	$16.50 \pm 0.04$	$11.51 \pm 0.04$	$1.92 \pm 0.04$	$0.47 \pm 0.04$	1
	$21.46 \pm 0.2$	$15.75 \pm 0.3$	$11.29 \pm 0.2$	...	...	2
	$25.10 \pm 0.70$	$15.50 \pm 0.88$	$10.85 \pm 0.83$	...	...	8
	$22.2 \pm 1.0$	$15.7 \pm 0.4$	$11.7 \pm 0.5$	$3.3 \pm 1.3$	$1.0 \pm 0.5$	14
HD 170740	$13.53 \pm 0.05$	$5.86 \pm 0.05$	$3.27 \pm 0.05$	$0.21 \pm 0.05$	...	1
	$13.60 \pm 0.43$	$6.68 \pm 0.61$	$3.82 \pm 0.60$	...	...	8
	$14.0 \pm 0.4$	$5.2 \pm 0.8$	$2.6 \pm 0.3$	...	...	14
HD 210121	$26.22 \pm 0.07$	$12.20 \pm 0.07$	$6.73 \pm 0.07$	$0.94 \pm 0.07$	$0.33 \pm 0.07$	1
	$27.9 \pm 1.8$	$10.5 \pm 1.6$	$4.5 \pm 1.0$	...	...	16
	$26.8 \pm 3.0$	$13.1 \pm 2.6$	$8.1 \pm 2.4$	...	...	17
	$23.4 \pm 2.0$	$10.0 \pm 0.9$	$4.9 \pm 0.9$	...	...	14

**References.** — (1) This Work; (2) Slyk et al. 2008; (3) Roth & Meyer 1995; (4) Kaiser et al. 1991; (5) Kaiser & Wright 1990; (6) Meyer & Jura 1985; (7) Pan et al. 2004; (8) Palazzi et al. 1992; (9) Federman et al. 1984; (10) Hawkins et al. 1993; (11) Crane et al. 1989; (12) Crane & Hegyi 1988; (13) Knauth et al. 2001; (14) Gredel et al. 1991; (15) Palazzi et al. 1990; (16) Sheffer (private communication); (17) Welty & Fowler 1992.

<sup>a</sup> Equivalent widths listed for HD 152236 and HD 154368 refer to the dominant velocity component. For the  $-4.8$  km s<sup>-1</sup> component toward HD 152236, we find  $W_\lambda R(0) = 1.64 \pm 0.06$ ,  $W_\lambda R(1) = 0.39 \pm 0.06$ , and  $W_\lambda P(1) = 0.14 \pm 0.06$ , while for the  $-13.9$  km s<sup>-1</sup> component toward HD 154368, we find  $W_\lambda R(0) = 0.28 \pm 0.04$  and  $W_\lambda R(1) = 0.09 \pm 0.04$ .

**Table 4**  
Adopted Molecular Line Parameters

Band	Line	$\lambda_{\text{air}}$ (Å)	$f$	Ref.
CN $B-X$ (0, 0)	$R(0)$	3874.608	0.0342	1
	$R(1)$	3873.998	0.0228	1
	$P(1)$	3875.763	0.0114	1
	$R(2)$	3873.369	0.0205	1
	$P(2)$	3876.310	0.0137	1
CN $B-X$ (1, 0)	$R(0)$	3579.963	0.0030	1
CH <sup>+</sup> $A-X$ (0, 0)	$R(0)$	4232.548	0.00545	2
CH <sup>+</sup> $A-X$ (1, 0)	$R(0)$	3957.692	0.00331	2

**References.** — (1) Roth & Meyer 1995; (2) Gredel et al. 1993.

**Table 5**  
CN Equivalent Width Ratios and Derived Column Densities and  $b$ -Values

Star	(0, 0) $R(1)/P(1)$	$N(N=1)^a$	$b^a$	(0, 0)/(1, 0) $R(0)$	$N(N=0)^a$	$b^a$
McDonald Sight Lines						
$\zeta$ Per	$1.98 \pm 0.11$	...	$\infty$	...	...	...
$\rho$ Oph A	$2.16 \pm 0.10$	...	$\infty$	$11.33 \pm 3.36$	...	$\infty$
$\zeta$ Oph	$1.74 \pm 0.17$	...	$\infty$	$11.59 \pm 1.54$	...	$\infty$
20 Aql	$2.01 \pm 0.10$	...	$\infty$	...	...	...
VLT/UVES Sight Lines						
HD 73882	$1.64 \pm 0.01$	$9.84 \pm 0.15$	$0.94 \pm 0.03$	...	...	...
HD 152236 (+6.0)	$1.91 \pm 0.10$	...	$\infty$	$13.28 \pm 3.26$	...	$\infty$
HD 154368 (+5.2)	$1.62 \pm 0.01$	$7.91 \pm 0.11$	$0.72 \pm 0.02$	$4.65 \pm 0.09$	$18.60 \pm 0.47$	$0.68 \pm 0.01$
HD 161056 (-3.1)	$1.86 \pm 0.04$	$1.67 \pm 0.10$	$0.52 \pm 0.30$	$15.64 \pm 3.01$	...	$\infty$
HD 161056 (+2.8)	$2.00 \pm 0.06$	...	$\infty$	$16.57 \pm 3.08$	...	$\infty$
HD 169454	$1.41 \pm 0.01$	$11.93 \pm 0.14$	$0.52 \pm 0.01$	$2.83 \pm 0.05$	$32.06 \pm 0.88$	$0.49 \pm 0.01$
HD 170740	$1.77 \pm 0.03$	$2.42 \pm 0.11$	$0.42 \pm 0.08$	$7.18 \pm 0.54$	$5.86 \pm 0.51$	$0.47 \pm 0.04$
HD 210121	$1.73 \pm 0.02$	$5.44 \pm 0.16$	$0.77 \pm 0.08$	$5.94 \pm 0.16$	$14.38 \pm 0.46$	$0.80 \pm 0.02$

<sup>a</sup> Column density (in  $10^{12} \text{ cm}^{-2}$ ) and  $b$ -value (in  $\text{km s}^{-1}$ ) derived from the measured equivalent width ratio for a pair of CN transitions arising from the same rotational state (either  $N=1$  or  $N=0$ ).



**Table 6**  
CH<sup>+</sup> and CN Component Structure

Star	CH <sup>+</sup>			CN		
	$v_{\text{LSR}}$ (km s <sup>-1</sup> )	$N^{\text{a}}$ (10 <sup>12</sup> cm <sup>-2</sup> )	$b$ (km s <sup>-1</sup> )	$v_{\text{LSR}}$ (km s <sup>-1</sup> )	$N^{\text{a}}$ (10 <sup>12</sup> cm <sup>-2</sup> )	$b^{\text{b}}$ (km s <sup>-1</sup> )
McDonald Sight Lines						
20 Tau	+7.4	17.93 ± 0.09	1.8	...	...	...
	+8.7	17.20 ± 0.09	1.8	...	...	...
23 Tau	+7.0	1.06 ± 0.08	2.7	...	...	...
	+10.0	18.42 ± 0.06	2.1	...	...	...
ζ Per	+6.7	3.16 ± 0.08	2.2	+6.6	2.31 ± 0.02	0.93
ρ Oph A	+1.5	6.95 ± 0.07	1.8	+1.7	1.77 ± 0.01	0.42
	+3.2	8.89 ± 0.06	1.5	...	...	...
ζ Oph	-0.9	31.86 ± 0.08	2.0	-1.4	1.61 ± 0.02	0.60
	...	...	...	-0.2	0.45 ± 0.02	0.40
20 Aql	-6.6	0.50 ± 0.09	2.0	...	...	...
	+2.6	3.15 ± 0.10	2.4	+1.7	2.76 ± 0.02	1.34
VLT/UVES Sight Lines						
HD 73882	+5.6	19.57 ± 0.09	2.8	+5.7	27.66 ± 0.04	0.88
	+10.2	2.39 ± 0.07	1.9	...	...	...
HD 152236	-16.9	0.85 ± 0.15	3.1	...	...	...
	-10.2	3.38 ± 0.12	2.0	...	...	...
	-2.0	11.07 ± 0.15	3.1	-4.8	0.38 ± 0.01	0.54
	+7.1	6.40 ± 0.14	3.0	+6.0	2.21 ± 0.02	0.40
HD 154368	-13.0	0.29 ± 0.06	1.9	-13.9	0.06 ± 0.01	0.20
	-6.8	0.90 ± 0.06	1.2	...	...	...
	+2.4	14.44 ± 0.07	2.1	...	...	...
	+6.6	7.29 ± 0.07	2.1	+5.2	18.19 ± 0.03	0.68 ± 0.01
HD 161056	-7.9	0.51 ± 0.15	4.3	...	...	...
	-3.2	0.77 ± 0.12	3.5	-3.1	3.34 ± 0.01	1.02
	+2.4	24.31 ± 0.13	3.8	+2.8	3.51 ± 0.02	2.00
HD 169454	-3.0	4.41 ± 0.08	4.2	...	...	...
	+5.5	14.96 ± 0.06	2.9	+5.7	30.92 ± 0.05	0.50 ± 0.01
	+15.4	1.16 ± 0.05	1.6	...	...	...
HD 170740	-1.1	0.51 ± 0.06	2.8	...	...	...
	+5.1	16.46 ± 0.07	3.1	+6.6	6.23 ± 0.02	0.46 ± 0.04
HD 210121	-7.4	2.82 ± 0.10	1.5	-6.7	14.33 ± 0.04	0.80 ± 0.02
	-2.7	8.33 ± 0.13	2.6	...	...	...

<sup>a</sup> Column densities refer to the <sup>12</sup>C-bearing isotopologue.

<sup>b</sup> We include 1-σ errors on  $b$ -values derived by means of the doublet ratio method (see § 3).

**Table 7**  
Total Molecular Column Densities and  $^{12}\text{C}/^{13}\text{C}$  Ratios

Star	$N(^{12}\text{CN})$ ( $10^{12} \text{ cm}^{-2}$ )	$^{12}\text{CN}/^{13}\text{CN}$	$\Delta v(\text{CN})$ ( $\text{km s}^{-1}$ )	$N(^{12}\text{CH}^+)$ ( $10^{12} \text{ cm}^{-2}$ )	$^{12}\text{CH}^+ / ^{13}\text{CH}^+$	$\Delta v(\text{CH}^+)$ ( $\text{km s}^{-1}$ )	$N(^{12}\text{CO})$ ( $10^{14} \text{ cm}^{-2}$ )	$^{12}\text{CO}/^{13}\text{CO}$	Ref.
McDonald Sight Lines									
20 Tau	0.06	...	...	$35.13 \pm 0.10$	$82.5 \pm 16.7$	-18.7	...	...	
23 Tau	0.03	...	...	$19.48 \pm 0.06$	$72.7 \pm 15.9$	-18.6	...	...	
$\zeta$ Per	$3.28 \pm 0.03$	$67.0 \pm 28.0$	+13.2	$3.16 \pm 0.08$	...	...	$17.9 \pm 0.5$	$108 \pm 5$	1
$\rho$ Oph A	$2.50 \pm 0.02$	$54.0 \pm 15.1$	+12.9	$15.84 \pm 0.08$	$64.7 \pm 18.5$	-19.0	$19.2 \pm 2.5$	$125 \pm 36$	1
$\zeta$ Oph	$2.89 \pm 0.03^a$	$48.8 \pm 19.5$	+13.0	$31.86 \pm 0.08$	$75.2 \pm 12.1$	-19.4	$25.4 \pm 1.6$	$167 \pm 25$	1
20 Aql	$3.94 \pm 0.04$	$62.1 \pm 22.2$	+12.8	$3.64 \pm 0.13$	...	...	$30^{+25}_{-15}$	$50 \pm 15$	2
VLT/UVES Sight Lines									
HD 73882	$38.44 \pm 0.06$	$85.0 \pm 3.3$	+12.6	$21.96 \pm 0.11$	...	...	$355 \pm 208$	$25 \pm 22$	3
HD 152236	$3.52 \pm 0.04^a$	$64.9 \pm 35.6$	+13.5 <sup>b</sup>	$21.70 \pm 0.28$	...	...	...	...	
HD 154368	$26.98 \pm 0.04$	$70.7 \pm 3.6$	+13.0	$22.91 \pm 0.13$	...	...	$26.7 \pm 5.5$	$37 \pm 8$	1
HD 161056	$10.10 \pm 0.04$	$36.3 \pm 3.5$	+14.0	$25.59 \pm 0.24$	...	...	...	...	
HD 169454	$44.73 \pm 0.06$	$68.7 \pm 1.3$	+12.8	$20.52 \pm 0.12$	...	...	...	...	
HD 170740	$8.77 \pm 0.03$	$133.6 \pm 33.0$	+13.4	$16.97 \pm 0.09$	...	...	...	...	
HD 210121	$19.77 \pm 0.05$	$68.4 \pm 4.9$	+13.3	$11.14 \pm 0.16$	...	...	$68 \pm 14$	$102 \pm 31$	3
Weighted mean		$67.5 \pm 1.0$	+13.1		$74.4 \pm 7.6$	-18.9			

**References.** — (1) Sheffer et al. 2007; (2) Hanson et al. 1992; (3) Sonnentrucker et al. 2007.

<sup>a</sup> Total  $^{12}\text{CN}$  column densities for  $\zeta$  Oph and HD 152236 do not include contributions from the  $N = 2$  level, but these contributions are likely to be small and within the uncertainties. If we assume  $T_{12} = T_{01}$ , we get  $N(N = 2) = 0.02 \times 10^{12} \text{ cm}^{-2}$  in both cases.

<sup>b</sup> The velocity shift for CN  $R(0)$  toward HD 152236 was held fixed during profile synthesis, and thus is not included in the mean.

**Table 8**  
Comparison between Column Densities Derived from the (0, 0) and (1, 0) Bands

Star	$N(\text{CH}^+)^a$		$N(\text{CN})^a$	
	(0, 0) $R(0)$	(1, 0) $R(0)$	(0, 0) $R(0)$	(1, 0) $R(0)$
McDonald Sight Lines				
20 Tau	$35.13 \pm 0.10$	...	...	...
23 Tau	$19.48 \pm 0.06$	$20.16 \pm 0.20$	...	...
$\zeta$ Per	$3.16 \pm 0.08$	...	$2.31 \pm 0.02$	...
$\rho$ Oph A	$15.84 \pm 0.08$	...	$1.77 \pm 0.01$	$1.53 \pm 0.48$
$\zeta$ Oph	$31.86 \pm 0.08$	$33.24 \pm 0.11$	$2.06 \pm 0.02$	$2.13 \pm 0.31$
20 Aql	$3.64 \pm 0.13$	...	$2.76 \pm 0.02$	...
VLT/UVES Sight Lines				
HD 73882	$21.96 \pm 0.11$	$22.50 \pm 0.26$	$27.66 \pm 0.04$	...
HD 152236	$21.70 \pm 0.28$	$21.42 \pm 0.49$	$2.59 \pm 0.03$	$2.36 \pm 0.82$
HD 154368	$22.91 \pm 0.13$	$22.89 \pm 0.24$	$18.25 \pm 0.04$	$18.59 \pm 0.38$
HD 161056	$25.59 \pm 0.24$	$27.05 \pm 0.42$	$6.85 \pm 0.02$	$5.44 \pm 0.84$
HD 169454	$20.52 \pm 0.12$	$21.14 \pm 0.20$	$30.92 \pm 0.05$	$30.78 \pm 0.52$
HD 170740	$16.97 \pm 0.09$	$17.62 \pm 0.21$	$6.23 \pm 0.02$	$5.64 \pm 0.41$
HD 210121	$11.14 \pm 0.16$	$10.98 \pm 0.40$	$14.33 \pm 0.04$	$13.42 \pm 0.38$

<sup>a</sup> Total (line-of-sight) column densities (in  $10^{12} \text{ cm}^{-2}$ ) derived through profile synthesis of the (0, 0) and (1, 0)  $R(0)$  lines in  $\text{CH}^+$  and CN.

**Table 9**  
CN Rotational Column Densities and Excitation Temperatures

Star	$N(N=0)$ ( $10^{12}$ cm <sup>-2</sup> )	$N(N=1)$ ( $10^{12}$ cm <sup>-2</sup> )	$N(N=2)$ ( $10^{12}$ cm <sup>-2</sup> )	$T_{01}$ (K)	$T_{12}$ (K)	$T_{01}(^{13}\text{CN})$ (K)
McDonald Sight Lines						
ζ Per	2.31 ± 0.02	0.94 ± 0.02	0.04 ± 0.02	2.723 ± 0.031	2.931 ± 0.411	...
ρ Oph A	1.77 ± 0.01	0.68 ± 0.01	0.04 ± 0.01	2.657 ± 0.026	3.136 ± 0.323	...
ζ Oph	2.06 ± 0.02	0.82 ± 0.02	...	2.702 ± 0.042	...	...
20 Aql	2.76 ± 0.02	1.12 ± 0.02	0.06 ± 0.02	2.728 ± 0.028	3.155 ± 0.340	...
VLT/UVES Sight Lines						
HD 73882	27.66 ± 0.04	10.48 ± 0.02	0.31 ± 0.02	2.631 ± 0.004	2.693 ± 0.038	2.706 ± 0.200
HD 152236 (-4.8)	0.38 ± 0.01	0.12 ± 0.02	...	2.454 ± 0.178	...	...
HD 152236 (+6.0)	2.21 ± 0.02	0.81 ± 0.02	...	2.588 ± 0.033	...	...
HD 154368 (+5.2)	18.19 ± 0.03	8.40 ± 0.02	0.29 ± 0.01	2.911 ± 0.004	2.815 ± 0.033	2.781 ± 0.192
HD 161056 (-3.1)	3.34 ± 0.01	1.59 ± 0.02	0.10 ± 0.02	2.960 ± 0.018	3.333 ± 0.159	...
HD 161056 (+2.8)	3.51 ± 0.02	1.46 ± 0.02	0.10 ± 0.02	2.761 ± 0.020	3.383 ± 0.210	...
HD 169454	30.92 ± 0.05	13.30 ± 0.02	0.51 ± 0.01	2.804 ± 0.003	2.881 ± 0.017	2.599 ± 0.082
HD 170740	6.23 ± 0.02	2.44 ± 0.02	0.11 ± 0.02	2.672 ± 0.011	2.989 ± 0.123	...
HD 210121	14.33 ± 0.04	5.31 ± 0.02	0.13 ± 0.02	2.604 ± 0.007	2.589 ± 0.096	3.096 ± 0.383
Weighted mean				2.754 ± 0.002	2.847 ± 0.014	2.652 ± 0.069

**Table 10**  
Total Ca I and Ca II Equivalent Widths

Star	$W_\lambda(\text{Ca I})$ (mÅ)	$W_\lambda(\text{Ca II})$ (mÅ)	Ref.
α Leo	0.12 ± 0.03	0.59 ± 0.07	1
	...	≲ 0.4	2
α Vir	≲ 0.06	5.95 ± 0.12	1
	≲ 0.2	...	3
	...	5.4	4
	...	4.8 ± 0.1	2
	...	5.2	5
	...	5.7	6
	...	5	7

**References.** — (1) This Work; (2) Vallerga et al. 1993; (3) Welty et al. 2003; (4) Welty et al. 1996; (5) Lallement et al. 1986; (6) Hobbs 1978; (7) Hobbs 1975.